Numerical analyses of novel prefabricated structural wall panels in residential buildings based on laboratory tests in scale 1:1

Łukasz Skarżyński, Ireneusz Marzec, Krzysztof Drąg and Jacek Tejchman*

Faculty of Civil and Environmental Engineering, Gdańsk University of Technology, Gdańsk, Poland

lskarzyn@pg.edu.pl, irek@pg.edu.pl, drjk46@gmail.com, tejchmk@pg.edu.pl

Abstract: The paper presents experimental and numerical investigations on novel prefabricated composite building wall panels for residential building constructions. The wall panels were composed of reinforced concrete ribbed elements with the core from the EPS foam as the thermal insulation. The wall panels in the full-scale 1:1 were subjected to vertical loads. In the first step, the experiments were analysed with simple usual static methods. Next they were analysed numerically using the finite element method based on two different constitutive continuum models for concrete. First, an elasto-plastic model with the Drucker-Prager criterion defined in compression and with the Rankine criterion defined in tension was used. Second, a coupled elasto-plastic-damage formulation based on the strain equivalence hypothesis was used. In order to describe strain localization in concrete, both models were enhanced in a softening regime by a characteristic length of micro-structure by means of a non-local theory. A satisfactory agreement between the experiments and FE analyses was achieved. In addition the FE results with the non-local approach were compared with the crack band model.

Keywords: composite panels; damage mechanics; elasto-plasticity; EPS foam; non-local theory; reinforced concrete; crack band approach

1. Introduction

Nowadays, in order to diminish construction costs and to shorten construction time of residential buildings, different prefabricated systems are offered on the building market. Prefabricated buildings are building types which consist of several factory-built components or that are assembled on-site to complete the unit. In addition, the structural design may be improved through the development and application of composite elements. An attractive energy-saving construction system for residential buildings was proposed. It is composed of monolithic load bearing capacity reinforced concrete (RC) frames and prefabricated composite structural insulated slabs and wall panels consisted of reinforced

concrete (RC) and expanded polystyrene (EPS) (Sewaco System, www.sewaco.pl, Smakosz & Tejchman 2014, Skarzyński et al. 2017). The advantages of such a construction system are:

a) short time of a building process due to presence of prefabrication for slabs and walls during a construction process (3 times shorter time than a standard monolithic construction),

b) energy-saving due to the presence of RC and EPS (thermal conductivity coefficient of external envelopes is only 0.11-0.15 kW/m^{2}K),

c) high apparent sound reduction index R due to the presence of RC and EPS (R=33-34 dB),

d) good standard of finish.

The wall panels were composed of RC ribbed elements with the core from the EPS foam as the thermal insulation. The both materials (RC and EPS) were together constructed in a prefabricated factory. The panels were 6.6 m long and 3.0 m high with the total thickness of 0.30 m. The expanded polystyrene (EPS) foam core had the thickness of 0.12-0.23 m. In usual engineering design calculations of residential houses, it was assumed that all loads were carried by horizontal prefabricated slab panels supported on spatial monolithic longitudinal and transverse RC frames located on ground beams and footings. The slabs were dimensioned in the usual way as RC T-elements without EPS and composite wall panels by means of 2 simple approaches: the frame model (FM) and truss wall model (TWM). The residential buildings were constructed in the following way:

a) footing foundations and foundations walls were placed on a stable soil ground,

b) inner and outer prefabricated composite walls were mounted on foundation walls (they were temporarily supported during mounting),

c) ceiling slabs and balcony slabs (without additional loads) above ground floor were placed on walls,

d) composite elements were connected with monolithic reinforced longitudinal and transverse RC frames by means of vertical bars ϕ10 every 50 cm and stirrups ϕ10 every 15 cm,

e) attic prefabricated wall was mounted and connected with reinforcement of monolithic frames,

f) ceiling slabs above the attic walls were constructed and roof panels were mounted,

g) finishing works were done.

Our paper is experimentally and theoretically oriented. It focuses on studying the strength, deformability and failure of 3 large wall panels 6.6×3.0×0.3 m^3 (scale 1:1) under bending, based on full-scale laboratory tests in order to evaluate their real load bearing capacity. The walls were symmetrically loaded by 1 or 3 vertical forces and failed in a different way: a) due to the rapture failure of the lower panel reinforcement (panel '1'), b)

2

local concrete damage under the vertical force (panel '2') c) and reinforcement rupture in the frame beam (panel '3'). Initially the experimental results were compared with a theoretical formula for the bearing capacity of RC-elements. Next, the numerical deterministic evaluation of experimental results using two different continuum constitutive models for concrete (for comparison purposes) was conducted. First, an isotropic elasto-plastic model with the Drucker-Prager criterion defined in compression and with the Rankine criterion defined in tension was used. Second, an isotropic coupled elasto-plastic-damage formulation based on the strain equivalence hypothesis was used. In order to ensure mesh-independent FE results and to properly describe strain localization in concrete, both models were enhanced in a softening regime by a characteristic length of micro-structure by means of a non-local theory in the integral format. For reinforcement simulations, an associated elasto-perfectly plastic constitutive law was assumed. A slip-bond model was assumed. The FE results with the non-local approach were also compared with the crack band model (called also the mesh-dependent softening modulus model) that has been used in many engineering computations as a simple technique eliminating or reducing the sensitivity of numerical results to the size of finite elements in simulations that involve strain localization due to softening zones (Bazant and Oh (1983), Jirasek and Bauer (2012), Xenos and Grassl (2016)). It is based on the idea that the crack opening is transformed into inelastic strain by distributing it over an element length dependent zone in order to preserve the overall energy dissipated by a failure process. Strain localization (width, spacing and inclination of localization zones) in this model strongly depends on the mesh size.

The innovative points in this paper are twofold (beneficial for the optimum engineering design):

a) experimental investigations of very large novel composite building wall panels with and without door/window holes in the scale 1:1 under bending,

b) validation of two popular continuum approaches for concrete in order to describe the shear strength, deflection and pattern of localization zones in large RC elements ($6.6 \times 3.0 \times 0.3$ m^3) that were constructed under industrial conditions. The paper is a continuation of experimental and numerical results concerning slab panels (Skarżyński et al. 2017).

2. Laboratory full-scale tests on composite wall panels

Three different bending tests were performed for ribbed wall panels containing EPS from one side: one for a full prefabricated panel without a monolithic frame (called wall panel '1', Figure 1a), second for a full prefabricated panel including a monolithic frame along edges (2 columns and 1 beam) (called wall panel '2', Figure 1b) and third for a prefabricated panel with a window and door hole including a monolithic frame on edges (2 monolithic columns and 1 beam) (called wall panel '3', Figure 1c). The panel concrete was prepared from the ordinary Portland cement (CEM I 42.5R), aggregate and water. The river sand and gravel aggregate was used with the maximum aggregate diameter

d_{max}=8 mm, mean aggregate diameter d_{50}=2 mm and aggregate volume of β=75%. The water to cement ratio was equal to w/c=0.42. The average cylinder compressive strength of panel concrete was f_{cm}=58.1 MPa, average splitting tensile strength f_{ctm}=3.97 MPa and average modulus of elasticity E_c=37.4 GPa. Frame concrete had the average cylinder compressive strength f_{cm}=47.1 MPa, average splitting tensile strength f_{ctm}=3.92 MPa and average modulus of elasticity E_c=36.7 GPa. The steel class was AIIIN (class B500). The concrete cover from the bar centre to the concrete surface was 20 mm. The yield strength of reinforcement was about 600 MPa and modulus of elasticity was E_s=200 GPa. The quasi-static tests were performed with the controlled displacement rate of 6-18 mm/h. The concentrated vertical loads were prescribed to the walls since concentrated forces (transferred from beams) provide the greatest load on walls.

Panel '1'

The full wall panel with 8 vertical ribs was free at ends. Its span was 6200 mm. The longitudinal bending reinforcement of the prefabricated horizontal panel rib (lower part of the frame beam) was composed of 3 bars ϕ14 (bottom bars) and 1 bar ϕ10 (top bar) (Figure 2). As the rib shear reinforcement, 42 stirrups ϕ6 and 21 vertical bars ϕ10 were used which also served as a connection between the prefabricated wall panel and monolithic frame beam (stitching reinforcement). As the reinforcement of the prefabricated vertical edge panel ribs and bottom horizontal panel rib, the bar meshes with the diameter of 6 mm were used at the distance of 150 mm in the both directions. The wall panel was incrementally loaded in a symmetric way by 3 vertical forces applied through steel plates 300×300×15 mm³ on rubber pads which were at the distance of 2.5 m (Figures 3 and 4). The displacements under the forces *F1-F3* were controlled independently of each other in order to obtain the similar maximum forces.

Figure 5 presents the experimental total vertical force against the mid-span deflection curve F=f(u) and crack pattern. The maximum total vertical force was F_{max}=F_1+F_2+F_3=221.4 kN for u≈3 mm (Figure 5A). Up to this force, the similar vertical forces were observed. For F=F_{max}, the first bending crack appeared at the mid-span which quickly propagated towards the panel top (Figure 5B). After it, the forces were different (the force F_1 fell down to 43 kN). The acceleration of the force F_2 allowed for equalizing the vertical forces to the value of 58 kN (u=5.2 mm). Next the force F_1 diminished due to the rupture failure of the lower panel reinforcement. Before cracking the horizontal and vertical wall displacements were not greater than 0.1 mm. After cracking the lower and upper wall part moved out of plane by about 2.7 mm. The maximum measured total vertical force F=221.4 kN was significantly higher than the maximum vertical assembly force on the building site for one panel 6.6 m wide, i.e. 83.6 kN.

Panel '2''

The full wall panel with 8 vertical ribs (as in the panel '1') was fixed in a monolithic frame (Figure 1b). The panel span was 6.6 m. The reinforcement of the prefabricated panel was the same as in the panel '1' (Figure 1a). The monolithic frame beam was reinforced with 2 longitudinal bars ϕ10 and frame columns were reinforced with 4 vertical bars ϕ12 and

stirrups with the diameter 6 mm placed at the distance of 150 mm (Figure 6). Moreover 2 bars $\phi14$ were used in two corners to link the monolithic frame beam and frame column reinforcement. The panel was incrementally loaded in a symmetric way by 1 vertical force applied through a steel plate on a rubber pad at the mid-span.

Figure 7 presents the experimental force-deflection curve $F=f(u)$ and crack pattern. The maximum failure force was $F_{max}=501.6$ kN for $u=3.1$ mm (Figure 7A). The first bending crack (Figure 7B) appeared in the slab mid-span for 25% of the maximum vertical force. Then it evolved towards the top and ended about 0.30 m below the prefabricated panel beam for the maximum force (its width was 0.35 mm). The panel failure took place in a rapid brittle way due to a local damage of concrete under the vertical force (Figure 8) - the longitudinal reinforcement has not yielded yet.

The lower and upper mid-part of the wall panel moved out of plane in different directions (1.3 mm at the upper part, 4.7 mm at the mid-part and 10 mm at the lower part). A visible jump in measured displacements was noticed after concrete cracking. The measured displacement of the columns was 0.4 mm (upper part) and 0.9 mm (mid-part).

Panel '3'

The wall panel with 7 vertical ribs had a window and door hole and was fixed in a monolithic frame (Figure 1c). The panel span was 6.6 m. The longitudinal reinforcement in the prefabricated upper horizontal panel rib was 2 bars $\phi10$ (bottom bars) and 1 bar $\phi10$ (top bar). As the shear reinforcement, the stirrups $\phi6$ at the distance 300 mm were used. In addition, the vertical bars $\phi10$ were put at the distance of 300 mm were used to preserve the connection between the prefabricated panel and monolithic frame beam (stitching reinforcement). As the reinforcement of the edge vertical panel ribs and lower horizontal panel rib, the bar meshes with the diameter 6 mm were used at the distance of 150 mm in the both directions. The monolithic frame beam was reinforced with 2 longitudinal bars $\phi10$ and the columns were reinforced with 4 vertical bars $\phi10$ and stirrups with the diameter 6 mm placed at the distance of 0.3 m (Figure 9). Moreover 2 bars $\phi12$ were used in two corners to link the monolithic beam and column reinforcement. The panel was symmetrically loaded from the top as the wall panel '2'.

Figures 10 and 11 present the experimental force-deflection curve $F=f(u)$ and crack evolution. The first peak of the vertical force was $F=108$ kN for $u=4.3$ mm. The maximum vertical force (second peak) was $F_{max}=118$ kN for $u=9.2$ mm (Figure 11). The deflection was calculated as the difference between the displacement of the mid-span bottom point and settlement of the supports. The experimental force indicated softening after the first peak of the vertical force, then re-hardening, second peak of the vertical force and again softening. The first softening appeared during the crack formation between the window and door. The prefabricated panel had the initial crack 0.1 mm wide in the window corner which was created during transportation. For the 25% of the maximum vertical force, the bending cracks first appeared in the panel mid-span. For $F=70$ kN and $u=1.83$ mm, three cracks occurred: one at the lower left window corner, second at the bottom at the mid-span and third in the upper door corner. For $F>70$ kN, a rapid growth of the width of the above cracks was noticed. For $F=80$ kN and $u=2.19$ mm,

the cracks were about 1 mm wide. For F=108 kN (u=4.3 mm), the panel part between the door and window was totally debonded and the load started to be carried by the frame only. For the maximum force F=118 kN (u=9.2 mm), the numerous cracks were observed: in the mid-span of the panel upper beam and frame beam, in the left frame corner and outside of the left frame column (Figure 11c). The wall panel failure took place in a rapid way due to the reinforcement rupture in the frame beam for u=11 mm.

In all experiments the measured cracking and failure forces for concentrated loads were higher than the calculated ones that corresponded to service uniformly distributed loads for residential buildings.

3. Initial dimensioning of wall panels

The bearing capacity of 3 composite wall panels was initially nvestigated with 2 simple usual approaches to dimension RC structures: the frame model (FM) and truss wall model (TWM). The FM approach was consistent with the dimensioning assumption for the building system, i.e. all loads were carried first by prefabricated slabs and then by monolithic RC frames. In TWM, the wall panels were modelled by sets of compressive and tensile rods. We assumed the actual cross-section geometry of vertical and horizontal ribs and beams. Concrete between ribs was replaced by diagonal rods with the rectangular cross-section of $b_r \times t$ (b_r=8t, t=40 mm - the concrete thickness). The concrete rods were removed when their cross-sections were cracked.

Panel '1'

In FM, the bending bearing capacity of the upper frame rib was calculated as a continuous beam supported on 8 elastic supports (vertical ribs). The external supports (imitating frame corners) were fixed. The calculated maximum bending span moment was 58 kNm. The maximum bending moment of the upper rib with the existing reinforcement was M=78.2 kNm (ΣF_i=109.1 kN).

The calculated moments and forces using TWM for the maximum total vertical force (F_1=80 kN, F_2=65 kN, F_3=75 kN) are depicted in Figures 12b and 12c. The calculated maximum bending moment of the horizontal upper frame rib was M_{max}=18.3 kNm (Figure 12b) and the maximum compressive normal force was N_{max}=-56.3 kN (Figure 12c). The corresponding bending moments and compressive normal forces were in the horizontal bottom panel rib: M=0 kNm, N=-58.7 kN and in the columns: M=0.94 kNm, N=-55.4 kN (Figures 12b and 12c). The characteristic design tensile resistance of the horizontal bottom panel rib (area 0.06×0.18 m^2, reinforcement 2ϕ6) was N_{Rd}=52.2 kN which was smaller than the experimental one of 58.7 kN. Thus, the wall panel was able to carry also the part of the horizontal tensile force.

Panel '2'

In the experiments the cracking force was 134 kN and failure force was 501.6 kN. The characteristic design moment resistance of the frame beam was M_{Rd}=124.9 kNm (caused

6

by the force F=113 kN). The maximum characteristic load on the panel during the building assembly was 115.9 kN.

In TWM (Figure 13a), for the experimental cracking force of 134 kN, the tensile force in the bar '12-13' was equal 30.6 kN. The tensile load bearing capacity of this bar was 40.7 kN. After a vertical crack occurred, the static scheme of the lattice wall has changed. The truss rod at the bottom central part (rod '12-13') did not transfer a normal force and the rod '5-13' did not transfer a shear force (Figure 13a). The critical section was the upper rod subjected to the eccentric compression. There, the calculated maximum bending moment (for F_{max}=501 kN) was M_{max}=150.38 kNm with the corresponding normal force N=-225.13 kN (Figures 14b and 14c). In turn, the bending moment and the normal force calculated based on the measured strains in concrete and reinforcement ($2\phi10$ and $3\phi14$), 34.6 kNm and 71.4 kN, were significantly smaller than from TWM. Thus TWM was not accurate enough to properly describe the distribution of the moment and forces after cracking and to reproduce the failure force.

Panel '3'

For FM the critical design resistance was the bending resistance of the upper beam M_{Rd}=76.7 kNm (F=61.7 kN). The shear resistance (stirrups $\phi10$ at the distance of 0.30 m) was V_{Rd}=170 kN (F=336 kN). The maximum characteristic panel load was 61.7 kN. The cracking occurred in the experimental panel for F=65 kN at the connection between the panel and upper beam in the region between a window and door and the failure force was 118 kN.

The initial (before cracking) static system for TWM is shown in Figure 15. In the experiment the initial crack appeared along the rod '2' in the nodes '8-9' for F=65 kN. In TWM the crack appeared in the node '8' for F=63 kN. The calculated bending moment in the upper beam (node '8') was 25.8 kNm (Figure 15b); in the laboratory test the bending moment was 25 kNm. After cracking, the model was modified, i.e. the rods '7' and '23' were assumed to be discontinuous and the rods '21' and '7' transferred compression only (Figure 16a). For the failure force F=118 kN, the maximum compressive normal force was N=-43.26 kN (left column). In the upper beam, the bending moment and normal force were M=76.02 kNm and N=-38.01 kN (Figures 16b and 16c) whereas the bending moment was 82 kNm in the laboratory test. The calculation deformation by TWM was approximately in agreement with the measured one.

For all wall panels a good agreement was obtained with respect to the cracking force. In order to calculate the failure load, a modified lattice wall model should be used by taking cracking into account. A satisfactory agreement was achieved for the panels '1' and '3'.

4. Constitutive models for concrete, reinforcement and EPS

The FE analyses were carried out with the most sophisticated wall panel '3'. Two different constitutive models for concrete were used: an isotropic elasto-plastic model (Equations (A1)-(A6), Appendix 1) and an isotropic coupled elasto-plastic-damage model (Equations (A7)-(A14), Appendix 2).

7

4.1. Elasto-plastic model for concrete

This isotropic elasto-plastic model for concrete (Marzec et al., 2007, Majewski et al., 2008, Tejchman & Bobiński, 2012, Korol et al., 2014) requires two elastic parameters: modulus of elasticity E and Poisson's ratio v, one compression yield stress function $\sigma_c=f(\kappa_1)$ (based on a uniaxial compression test), one tensile yield stress function $\sigma_t=f(\kappa_2)$ (based on a uniaxial tension test), internal friction angle φ and dilatancy angle ψ (based on a triaxial compression test). The model has some disadvantages. The shape of the failure surface in a principal stress space is linear (not paraboloidal as in reality). In deviatoric planes, the shape is circular (during compression) and triangular (during tension); thus it does not gradually change from a curvilinear triangle with smoothly rounded corners to nearly circular with increasing pressure. The strength is similar during triaxial compression and extension, and the stiffness degradation due to strain localization and non-linear volume changes during loading are not taken into account.

The following material parameters were assumed (for the prefabricated panel and monolithic frame): E=37.1 GPa and v=0.20 (based on laboratory experiments). The cylinder compressive strength was f_c=52.6 MPa and tensile strength was f_t=3.94 MPa (based on the laboratory experiments). The linear relationship between the compressive σ_c and hardening/softening parameter κ_1 was assumed. We assumed 3 different linear hardening/softening curves (Figure 17A). The compressive fracture energy G_c was equal to 2750 N/m (curve 'a', κ_1^{res}=0.003), 3250 N/m (curve 'b', κ_1^{res}=0.003) or 3750 N/m (curve 'c', κ_1^{res}=0.0055). It was calculated as $G_c=g_c{\times}w_c$ (g_c - area under the entire softening/hardening function up to κ_1=0.006, $w_c{\approx}3.5{\times}l_c$ - the width of compressive localization zones with l_c=5 mm, Tejchman & Bobiński, 2012). In the case of the tensile fracture energy, two non-linear exponential Hordijk's curves were analysed (Figure 17B). The tensile fracture energy G_f varied between 200 N/m (curve 'a') and 400 N/m (curve 'b'). It was calculated as $G_f=g_f{\times}w_f$ (g_f - area under the entire softening function, $w_f{\approx}3.5{\times}l_c$ - the width of tensile localization zones with l_c=5 mm). The ratio G_c/G_f was approximately 15. The internal friction angle was equal φ=12° (Eq.A2), dilatancy anlgle ψ=8° and non-locality parameter m=2 (Bobiński & Tejchman, 2004).

4.2. Coupled elasto-plastic damage model for concrete

The constitutive model (Marzec & Tejchman, 2012, 2013, Skarżyński et al., 2017) assumes the different stiffness in tension and compression and a positive-negative stress projection operator to simulate crack closing and crack re-opening and is thermodynamically consistent. It shares main properties of the model by Lee & Fenves (1998), which was proved to not violate thermodynamic principles (plasticity is defined in the effective stress space, isotropic damage is used and the stress weight function is similar). Moreover Carol & Willam (1996) showed that for damage models with crack-closing-re-opening effects included, only isotropic formulations did not suffer from spurious energy dissipation under non-proportional loading (in contrast to anisotropic ones). The constitutive model shares properties of other coupled elasto-plastic-damage

formulations for concrete (Chen et al., 2012, Grassl et al., 2013, Mihai et al., 2016, Xotta et al., 2016).

The coupled elasto-plastic-damage model requires the following 12 material constants E, υ, κ_0, α, β, η_1, η_2, δ, a_t, a_c, ψ and φ and 2 hardening yield stress functions (the function by Rankine in tension and the function by Drucker-Prager in compression). In the case of linear hardening, 16 material constants are totally needed (E, υ, κ_0, α, β, η_1, η_2, δ, a_t, a_c, ψ, φ, initial yield stresses σ_{yt}^0 (tension) and σ_{yc}^0 (compression) and hardening plastic moduli H_p in compression and in tension). If the tensile failure prevails, one yield stress function by Rankine can be used only. The quantities σ_y^0 (initial yield stress during hardening) and κ_0 are responsible for the peak location on the stress-strain curve and a simultaneous activation of a plastic and damage criterion (usually the initial yield stress in the hardening function σ_{yt}^0=3.5-6.0 MPa and κ_0=(8-15)×10⁻⁵ under tension). The shape of the stress-strain-curve in softening is influenced by the constant β in tension (usually β=50-800), and by the constants δ and η_2 in compression (usually δ=50-800 and η_2=0.1-0.8). The parameter η_2 influences also a hardening curve in compression. In turn, the stress-strain-curve at the residual state is affected by the constant α (usually α=0.70-0.95) in tension and by η_1 in compression (usually η_1=1.0-1.2). Since the parameters α and η_1 are solely influenced by high values of κ, they can arbitrarily be assumed for softening materials. Thus, the most crucial material constants are σ_y^0, κ_0, β, δ and η_2. In turn, the scale factors a_t and a_c influence the damage magnitude in tension and compression. In general, they vary between zero and one. There do not exist unfortunately the experimental data allowing for determining the magnitude of a_t and a_c. Since, the compressive stiffness is recovered upon the crack closure as the load changes from tension to compression and the tensile stiffness is not recovered due to compressive micro-cracks, the parameters a_c and a_t can be taken for the sake of simplicity as a_c=1.0 and a_t=0 for many different simple loading cases as e.g. uniaxial tension and bending. The equivalent strain measure $\tilde{\varepsilon}$ was defined in terms of elastic strains. In uniaxial compression, the material strength increases with increasing κ_0 and decreasing δ and η_2 and the material softening grows with increasing κ_0 and decreasing η_2. The material softening mainly increases with decreasing β. The drawback of this formulation is the necessity to tune up constants controlling plasticity and damage to activate an elasto-plastic criterion and a damage criterion at the same moment. As a consequence, the chosen initial yield stress σ_y^0 may be higher than this obtained directly in laboratory simple monotonic experiments.

Within the elasto-plastic-damage, the FE calculations were mainly performed with the following set of material parameters: σ_{yt}^0=4.6 MPa (tension), σ_{yc}^0=54 MPa (compression), H_p=21 GPa (in both tension and compression), κ_0=1.10×10⁻⁴, φ=14º, ψ=8º, β=100, α=0.90, η_1=1.05, η_2=0.38, δ=450, a_t=0 and a_c=1. In addition, the computations were carried out with the smaller tensile fracture energy (β=700).

4.3. Non-local approach for concrete

Standard constitutive laws are not able to describe properly strain softening of the material when using FEM that results in pathological sensitivity of the numerical solution to the size and alignment of finite elements. Since these laws contain no information about the size and spacing of localization zones, their enrichment by a characteristic length of micro-structure (related to the size and spacing of material heterogeneities) is necessary. The characteristic length restores also the well-posedness of boundary value problems and makes the FE results mesh-independent. A non-local theory in the integral format was used as a regularisation technique (Bažant & Jirásek, 2002, Tejchman & Bobinski, 2012, Bobiński & Tejchman, 2016, Giry et al., 2011, Pijauder-Cabot & Dufour, 2010). In this approach, the principle of a local action does not take place any more. Polizzotto et al. (1998) laid down a thermodynamically consistent formulation of non-local plasticity. In the calculations, the softening parameters κ_i (i=1, 2) were assumed to be non-local (independently for both yield surfaces f_i) (Brinkgreve, 1994)

$$\bar{\kappa}_i(\boldsymbol{x}) = (1-m)\kappa_i(\boldsymbol{x}) + m\frac{\int_V \omega(\|\boldsymbol{x}-\boldsymbol{\xi}\|)\kappa_i(\boldsymbol{\xi})\mathrm{d}\boldsymbol{\xi}}{\int_V \omega(\|\boldsymbol{x}-\boldsymbol{\xi}\|)\mathrm{d}\boldsymbol{\xi}} \qquad \text{for} \qquad i\text{=1, 2} \qquad (1)$$

where $\bar{\kappa}_i(\boldsymbol{x})$ are the non-local softening parameters, V denotes the body volume, $\boldsymbol{x}$ is the coordinate vector of the considered point, $\boldsymbol{\xi}$ is the coordinate vector of the surrounding points, ω denotes the weighting function and m is the additional non-local parameter controlling the size of the localization plastic zone. In the calculations within and coupled elasto-plastic-damage, the equivalent strain measure $\tilde{\varepsilon}$ was replaced by its non-local definition (Marzec & Tejchman, 2012)

$$\bar{\varepsilon} = \frac{\int_V \omega(\|\boldsymbol{x}-\xi\|)\tilde{\varepsilon}(\xi)d\xi}{\int_V \omega(\|\boldsymbol{x}-\xi\|)d\xi}. \qquad (2)$$

As a weighting function ω, the Gauss distribution function was used (Bažant & Jirásek 2002)

$$\omega(r) = \frac{1}{l_c\sqrt{\pi}}e^{-\left(\frac{r}{l_c}\right)^2} \qquad (3)$$

where l_c is a characteristic length of micro-structure and the parameter r is the distance between material points. The averaging in Equation (1) was restricted to a small representative area around each material point (the influence of points at the distance of r=3×l_c was only of 0.01%). Some different techniques (e.g. symmetric local correction approach, distance-based and stress-based model) may be used to calculate softening non-local parameters near boundaries in order to remove an excessive energy dissipation (particularly pronounced for notched specimens) (Borino et al. 2002, Grassl et al. 2014, Jirasek et al. 2016). The distance-based model seems to be the most realistic since it provides a good agreement for both unnotched and notched beams with the same set of parameters (Havlasek et al. 2016). In our paper, due to a large wall panel size and a small

10

effect of boundaries, the softening non-local parameters near boundaries were calculated using a standard formulation (Eqs.1-3) (Bažant & Jirásek, 2002). When calculating non-local quantities close to notches, the so-called "shading effect" is considered (Bažant & Jirásek, 2002), i.e. the averaging procedure considers the notches as an internal barrier that is shading a non-local interaction.

The characteristic length l_c is mainly determined with an inverse identification process of experimental data (Mahnken & Kuhl 1999, Skarżyński et al. 2011). In order to simplify the calculations, non-local rates were replaced by their approximations calculated with known total strain increments (Brinkgreve 1994). The characteristic length l_c of micro-structure within isotropic elasto-plasticity and isotropic damage mechanics may be about 2 mm (fine-grained concrete) and 5 mm (usual concrete). based on the image correlation DIC results (Skarżyński et al. 2011, Skarżyński & Tejchman 2010, 2013). We assumed l_c=5 mm in our FE analyses. Note that in order to obtain totally mesh-independent results, the mesh size should be smaller or equal to (2-3)×l_c (Tejchman & Bobiński 2012). The FE calculations with a local approach totally depend on the mesh size (load-displacement curves and strain localization) (Tejchman and Bobinski, 2012, Skarżyński et al. 2017).

4.4. Reinforcement

In order to simulate the behaviour of main reinforcement bars and stirrups (modelled as one-dimensional truss elements), the elasto-perfect plastic constitutive law was assumed with the following E_s=200 GPa (modulus of elasticity) and σ_y^s=600 MPa (σ_y^s – yield steel stress). The calculations were mainly carried out with bond-slip. In the first case, the same displacements along a contact surface/line between concrete and reinforcement were assumed. In the case of bond-slip, the analyses were carried out with a relationship between the bond shear stress τ_b and slip u using the simplest bond law Dörr (Tejchman & Bobiński, 2012) which neglected softening and assumed a yield plateau:

$$\tau_b = f_t\left[0.5\left(\frac{u}{u_0}\right) - 4.5\left(\frac{u}{u_0}\right)^2 + 1.4\left(\frac{u}{u_0}\right)^3\right] \qquad if \quad 0 < u \le u_0$$
$$\tau_b = 1.9 f_t \qquad\qquad\qquad if \quad u > u_0 \qquad (4)$$

The parameter u_0 is the displacement at which perfect slip occurs. In order to consider bond-slip, the interface with a zero thickness was assumed along a contact surface/line where a relationship between the shear traction and slip was introduced. The calculations were carried out with the bond-slip for u_0=0.03-1.0 mm.

The two 3D enhanced models were implemented into the commercial finite element code Abaqus (2011) with the aid of the subroutine UMAT (user constitutive law definition) and UEL (user element definition) for efficient computations (Bobiński & Tejchman, 2004). For the solution of a non-linear equation of motion governing the response of a system of finite elements, the initial stiffness method was used with a symmetric elastic global stiffness matrix. The calculations were carried out using the

11

Abaqus finite element code (Abaqus, 2011). The non-local averaging was performed in the current configuration. This choice was governed by the fact that element areas in this configuration were automatically calculated in Abaqus (2011).

Both isotropic constitutive concrete models of Sections 4.1 and 4.2 were several times used to successfully simulate fracture and strength in different RC elements subjected to shear and bending (e.g. Bobiński and Tejchman, 2004, Tejchman and Bobinski 2012, Marzec, et al. 2007, Marzec and Tejchman, 2012, 2013, Marzec et al. 2013, Skarzynski et al. 2017, Korol et al. 2014, 2017). For simulations of curved cracks during the so-called mixed shear-tension test by Nooru-Mohamed, the isotropic elasto-plastic model with the Rankine criterion and non-local softening was found to be the most suitable approach for a realistic simulation of the experimental cracks' shape and curvature (Bobiński and Tejchman, 2016a, 2016b). The results produced with an isotropic damage formulation were less realistic and strongly depended upon the equivalent strain definition (Bobiński and Tejchman, 2016a).

5. FE results for composite wall panel

The numerical simulations were solely carried out for the wall panel '3' (with a window and door opening) that was fixed to the monolithic RC frame. Approximately 600'000 tetrahedral elements were used (Figure 18). Each four-node tetrahedron included linear interpolation functions. The element width and height were equal to $s=30$ mm (i.e. $s=6×l_c$ with $l_c=5$ mm) and element depth was 20-30 mm [$s=(4-6)×l_c$]. The reduction of the element size down to the recommended value of $s=(2-3)×l_c$ (in order to properly capture strain localization) was not performed in order to reduce to diminish the computation time. In the case of FE calculations of non-local interactions in all panel finite elements, the computation time was about 3.5 weeks using the computer with the Intel Xeon CPU 3.10 GHz (2 processors), 128 GB RAM and 64-bit system. For calculations of non-local interactions in neighbouring elements only, the computation time was reduced to 9 days for one panel. Since preliminary computations indicated that the influence of EPS on the panel strength and distribution of localization zones was negligible (Skarżyński et al. 2017), the FE calculations were carried out without EPS. The effect of the compressive fracture energy of Figure 17A also did not affect the results.

5.1 FE results within enhanced elasto-plasticity

The calculated force-deflection curves in the composite wall panel for the different bond-slip between steel and reinforcement of Equation (4) ($u_o=0-1$ mm) and 2 different tensile fracture energies of Figure 17B ($G_f=200-400$ N/m) are presented in Figures 19-21 without the wall weight ($G_c=2750$ N/m (curve 'a' of Figure 17A), $l_c=5$ mm).

The calculated vertical force always increased with increasing tensile fracture energy G_f (Figure 20). For $G_f=200$ N/m, the calculated maximum vertical force $F=108$ kN ($u=10.5$ cm) was smaller by 10% than the experimental one, whereas for $G_f=400$ N/m,

the calculated maximum vertical force F=140 kN for the deflection u=13.7 cm was higher by 20% than the experimental one (Figure 20). The bond stiffness reduction (expressed by the growth of u_0) reduced two peak vertical forces and increased the number of localization zones (Figure 19). The calculated begin of re-hardening was too far for u_o≤0.06 mm and too close for u_o=1 mm as compared to the experiment (Figure 19). The first softening on the force-deflection curve (Figures 19 and 20) occurred when two localization zones developed between the window and door. When the region between the window and door had its maximum strength, the frame started to carry the load and the re-hardening took place on the force-deflection curve (Figures 19 and 20).

The calculated load-deflection curves, without the wall weight, in the composite wall panel for 3 different compressive fracture energies of Figure 17A (G_c=2750-G_c=3750 N/m) are presented in Figure 22 (G_f=200 N/m, curve 'a' of Figure 17B, l_c=5 mm). The calculated maximum vertical force slightly increased with increasing G_c. The constants G_c and κ_1^{res} of Figure 17A strongly affected the moment of re-hardening on the load-deflection curve. For G_c=2750 N/m and κ_1^{res}=0.003 (curve 'a' of Figure 17A), the material re-hardening started for u=6.2 cm whereas for G_c=3250 N/m and κ_1^{res}=0.003 (curve 'b' of Figure 17A) it started earlier for u=5.6 mm. The best satisfactory agreement between the calculations and experiments with respect to both peak vertical forces and shape of the force-deflection curve (curve 'c' in Figure 22) was for G_c=3250 N/m and κ_1^{res}=0.003 (curve 'b' in Figure 17A), G_f=200 N/m (curve 'a' in Figure 17B) and u_o=0.03 mm.

The geometry and its evolution of the calculated localization zones (Figures 19 and 21) based on the distribution of the non-local equivalent strain measure was similar as the experimental crack pattern (Figure 11). However, some discrepancies happened in the calculations (Figures 19e and 21e). The inclination of the shear crack at the window bottom corner to the horizontal (35º) was too small as compared with the experiment (50º). A smaller number of localization zones was calculated at the panel left upper corner and above the window due to a too large FE size with respect to l_c. In addition, strain localization was computed at the panel right support that was not visible in the experiment. The vertical localization zone at the panel bottom region did not reach the panel bottom in contrast to experiments.

The wall panel failure took place in the experiment in a rapid way due to the reinforcement rupture in the frame beam, characterized by a drop in the load-displacement curve occurred at the experiment end in the range u=9.2-11 mm (Fig.10). Since the elasto-perfect plastic constitutive law was assumed for reinforcement in the numerical simulations, a yield plateau was finally obtained in the FE simulations at the test end (Figs.19, 20 and 22). The calculated maximum normal tensile stress in the upper beam reinforcement was at the mid-span 600 MPa (reinforcement yielded) whereas in the experiment was slightly higher, 620 MPa (Figure 23A). The calculated maximum compressive stress in concrete in the frame beam, 26.9 MPa, was larger by 20% than in the experiment (Figure 23B).

13

5.2 FE results within enhanced coupled elasto-plastic damage

The results for the coupled elasto-plastic-damage model with a non-local softening (l_c=5 mm) using the bond-slip law (u_0=0.03 mm) are described in Figure 24. In addition the local results and the results using the crack band approach (limited to the tensile softening) were attached. In the crack band approach, the area under the stress–strain diagram, which represents dissipated energy per unit volume was adjusted in inverse proportion to the width of a localized failure zone. The new material constants were calibrated with the aid of a simple numerical 2D plain strain concrete three-point bending test with the size of finite elements equal to s=30 mm and G_f=170 N/m (as for the wall panel of Section 5). In order to obtain a close agreement with the non-local solution (that realistically describes the width of localization zones), the updated model constants β, η_2 and δ were assumed: β=70, η_2=0.32 and δ=350. Thus, the dissipated tensile energy per unit volume was the same in both the non-local and crack band approach for bending. For the crack band approach, the computation time was shorter by the factor 3 as compared to the non-local approach (with a non-local interaction related to neighbouring elements only).

The calculated ultimate vertical force ≈113 kN in the non-local approach differed by about 4% from the experimental value (118 kN) (Figure 24). The calculated minimum vertical force after the first peak (91 kN) and maximum force after the first minimum (113 kN) were also similar. The calculated localization zone geometry (Figure 24b) again matched satisfactorily the experimental cracks pattern (Figure 10). In contrast to the experiment, additional strain localization occurred close to the right panel support, the vertical localization zone did not occur above the window upper left corner, less localization zones occurred at the panel upper left corner and above the window (Figure 24b). Moreover the shear crack at the window bottom corner was too flat and the vertical localization zone at the panel bottom mid-region was too less developed. Thus the enhanced elasto-plastic solution (Figure 21e) was slightly more realistic than the enhanced elasto-plastic damage one (Figure 24b) as compared to the experiment.

For the crack band approach (Figure 24c), the force-deflection curve was similar as in the non-local approach (through a fit of the dissipated tensile energy per unit volume to the non-local solution). The widths of localization zones were mesh-dependent and limited to the sizes of finite elements. The arrangement of localization zones was less realistic than this in the non-local approach (Figure 24b). No localization zones occurred above the door and an additional vertical localization zone happened also at the window upper right corner in contrast to experiments (Fig.24c). Moreover, one central vertical localization zone above the window was not fully developed.

According to Jirasek and Bauer (2012), the practical application of the crack band approach as a technique eliminating the pathological mesh sensitivity is not straightforward since the success depends on many different factors (e.g. fracture energy rescaling, element type and element shape). Xenos and Grassl (2016) showed that both the load-displacement curves and crack patterns were however mesh-dependent for reinforced concrete elements using the crack band approach. In the case of the FE

14

analyses with the local-approach (Fig.24d), the force-deflection curve and strain localization were clearly different than in the non-local approach, depending upon the mesh-discretization.

The numerical normal stresses in tensile reinforcement and compressive concrete at the mid-span of the frame beam were in agreement with the experiment using the non-local approach (Figure 25). The decrease of the plastic modulus H_p changed the failure mechanism and lead to a higher maximum vertical force. It caused a slower increase of elastic strains and consequently a slower increase of the equivalent strain. Therefore the region between the window and door had a larger strength thus the frame started to carry the load later and thus the re-hardening effect was shifted. The localization zone in the central bottom wall part was more developed and less localization zones were in the frame.

Summarized the both enhanced constitutive continuum models for concrete satisfactorily captured the behaviour of the large wall panel under bending. Good accordance between the numerical and experimental outcomes was achieved with respect to the maximum vertical force, failure mode, location of localization zones and normal stresses in tensile reinforcement and compressive concrete. The differences between the experimental and calculated crack geometry were probably caused by the fact that concrete imperfections during element constructions were not taken into account during calculations (Section 2). In addition, the element size ($s=6{\times}l_c$) was twice as large as compared to l_c (the recommended value $s=3{\times}l_c$).

6. Conclusions

Based on the experimental and numerical investigations of novel composite building wall panels subjected to bending in the scale 1:1, the following conclusions can be drawn:

- For all experimental wall panels, both the cracking and failure forces were larger than the service load. The presence of wall panel openings strongly decreased (about 4 times) the wall panel's strength. The strength of the wall panel with the frame was two times higher then the strength of the pure wall panel. Large concentrations of tensile stresses occurred at opening corners and between the openings (door and window). Due to that the additional reinforcement close to openings (bar nets $\phi6$) and bottom panel bars ($2{\times}\phi10$) were recommended.

- For the wall panels '1' and '3', a good agreement was achieved between simple theoretical calculations of Section 3 and experiments. For the panel '2', a satisfactory agreement between theoretical calculations and experiments was solely obtained for the cracking force.

- Both constitutive continuum models with non-local softening for concrete satisfactorily reproduced the behaviour of the wall panel with openings under bending in spite of its large size and usual industrial realisation. The numerical outcomes were similar as the experimental ones with respect to the maximum

vertical force, shape of the force-deflection curve, failure mode, geometry of localization zones and normal stresses in tensile reinforcement and compressive concrete. The calculated vertical force always increased with increasing tensile and compressive fracture energy and bond stiffness. The tensile fracture energy, compressive fracture energy and residual compressive parameter strongly affected the moment of re-hardening on the force-deflection curve.

- Both the non-local and crack band approach produced similar force-deflection curves. The calculated geometry of cracks was however more realistic in the non-local approach. In the crack-band approach, the width of localization zones was strongly mesh-dependent and equal to the element size.

References

Abaqus Theory Manual, Version 6.11 (2011), Dassault Systèmes, 1080 Main Street, Pawtucket, RI 02860-4847, U.S.A.

Bažant, Z. P. and Jirasek, M. (2002). Non-local integral formulations of plasticity and damage: survey of progress. *Journal of Engineering Mechanics,* 128, 1119-1149.

Bažant, Z. P. and Oh, B. H. (1983). Crack band theory for fracture of concrete. *Mater. Struct.* 16, 155–177.

Bobiński, J. and Tejchman J. (2004). Numerical simulations of localization of deformation in quasi-brittle materials within non-local softening plasticity. *Computers and Concrete,* 1(4), 1-22.

Bobinski, J. and Tejchman, J. (2016a). Comparison of continuous and discontinuous constitutive models to simulate concrete behaviour under mixed mode failure conditions. *International Journal of Numerical and Analytical Methods in Geomechanics,* 40, 406-435.

Bobinski, J. and Tejchman, J. (2016b). A coupled constitutive model for fracture in plain concrete based on continuum theory with non-local softening and eXtended Finite Element Method. *Finite Elements in Analysis and Design,* 114, 1-21.

Borino G, Failla B, Parrinello F. (2002). A symmetric formulation for non-local damage models", In Mang HA, Rammerstorfer FG, Eberhardsteiner J. (eds). *Proceedings of the Fifth World Congress on Computational Mechanics (WCCM V)*, Vienna, Austria, 2002. Vienna University of Technology. ISBN 3-9501554-0-6, http://wccm.tuwien.ac.at.

Brinkgreve, R. B. J. (1994). Geomaterial models and numerical analysis of softening. *PhD Thesis*, Delft University of Technology.

Carol, I. and Willam, K. (1996). Spurious energy dissipation/generation in stiffness recovery models for elastic degradation and damage. *International Journal Solids Structures,* 33(20-22), 2939-2957.

Chen, J. F., Morozov, E. V. and Shankar, K. (2012). A combined elastoplastic damage model for progressive failure analysis of composite materials and structures. *Composite Structures*, 94, 3478–3489.

Giry, C., Dufour, F. and Mazars, J. (2011). Stress-based nonlocal damage model. *International Journal of Solids and Structures*, 48, 3431-3443.

Grassl, P., Xenos, D., Nyström, U., Rempling, R. and Gylltoft, K. (2013). CDPM2: A damage-plasticity approach to modelling the failure of concrete. *International Journal of Solids and Structures*, 50, 3805–3816.

Grassl, P., Xenos, D., Jirásek. M, and Horák, M. (2014). Evaluation of nonlocal approaches for modelling fracture near nonconvex boundaries. *Int. J. Solids Struct*., 51:3239–51.

Havlásek, P., Grassl, P. and Jirásek, M. (2016). Analysis of size effect on strength of quasi-brittle materials using integral-type nonlocal models. *Engineering Fracture Mechanics*, 72–85.

Jirasek, M. and Bauer, M. (2012). Numerical aspects of the crack band approach. *Computers and Structures* 110-111, 60-78.

Korol, E., Tejchman, J. and Mróz, Z. (2014). FE analysis of size effects in reinforced concrete beams without shear reinforcement based on stochastic elasto-plasticity with non-local softening. *Finite Elements in Analysis and Design*, *88*, 25-41.

Korol, E., Tejchman, J., Mroz, Z. (2017). Experimental and numerical assessment of size effect in geometrically similar slender concrete beams with basalt reinforcement. *Engineering Structures*, 141, 272-291.

Lee, J. and Fenves, G. L. (1998). Plastic-damage model for cyclic loading of concrete structures. *Journal of Engineering Mechanics,* 124(8), 892-900.

Majewski, T., Bobinski, J. and Tejchman, J. (2008). FE-analysis of failure behaviour of reinforced concrete columns under eccentric compression. *Engineering Structures,* 30(2), 300-317.

Mahnken, R. and Kuhl, E. (1999). Parameter identification of gradient enhanced damage models. *European Journal of Mechanics A/Solids,* 18, 819-835.

Marzec, I., Bobinski, J. and Tejchman, J. (2007). Simulations of crack spacing in reinforced concrete beams using elastic-plasticity and damage with non-local softening. *Computers and Concrete,* 4(5), 377-403.

Marzec, I. and Tejchman, J. (2012). Enhanced coupled elasto-plastic-damage models to describe concrete behaviour in cyclic laboratory tests: comparison and improvement. *Archives of Mechanics,* 64(3), 227-259.

Marzec, I. and Tejchman, J. (2013). Computational modelling of concrete behaviour under static and dynamic conditions. Bulletin Of The Polish Academy Of Sciences-Technical Sciences 61(1), 85-96.

Marzec, I., Skarżyński, Ł., Bobiński, J. and Tejchman, J. (2013). Modelling reinforced concrete beams under mixed shear-tension failure with different continuous FE approaches. *Computers and Concrete*, 12(5), 585-612.

Mazars, J. and Pijaudier-Cabot, G. (1996). From damage to fracture mechanics and conversely: a combined approach. *International Journal of Solids and Structures*, 33(20*)*, 3327-3342.

Mihai, I.C., Jefferson, A.D. and Lyons, P. (2016). A plastic-damage constitutive model for the finite element analysis of fibre reinforced concrete. *Engineering Fracture Mechanics*, doi: http://dx.doi.org/10.1016/j.engfracmech.2015.12.035.

Pamin, J. and de Borst, R. (1999). Stiffness degradation in gradient-dependent coupled damage-plasticity. *Archives of Mechanics*, 51(3-4), 419-446.

Peerlings, R. H. J., de Borst, R., Brekelmans, W. A. M. and Geers, M. G. D. (1998). Gradient enhanced damage modelling of concrete fracture. *Mechanics of Cohesive-Frictional Materials,* 3, 323-342.

Pijauder-Cabot, G. and Dufour, F. (2010). Non-local damage model boundary and evolving boundary effects. *European Journal of Environmental and Civil Engineering, 14*, 729-749.

Polizzotto, C, Borino, G. and Fuschi, P. (1998). A thermodynamically consistent formulation of nonlocal and gradient plasticity. *Mechanics Research Communications,* 25(1*)*, 75-82.

Sewaco System, patent implementations, PCT/PL2012/000076, P.396140, P.400541, P.400558.

Skarżyński, Ł. and Tejchman, J. (2010). Calculations of fracture process zones on meso-scale in notched concrete beams subjected to three-point bending. *European Journal of Mechanics/A Solids,* 29, 746-760.

Skarżyński, Ł, Syroka, E. and Tejchman, J. (2011). Measurements and calculations of the width of fracture process zones on the surface of notched concrete beams. *Strain,* 47, 319-332.

Skarżyński, Ł. and Tejchman, J. (2013). Experimental investigations of fracture process in plain and reinforced concrete beams under bending. *Strain*, 49(6), 521-543.

Skarżyński, Ł., Marzec, I., Tejchman, J. (2017). Experiments and numerical analyses for composite RC-EPS slabs. *Computers and Concrete*, 20 (6), 689-704.

Smakosz, Ł. and Tejchman, J. (2014). Evaluation of strength, deformability and failure mode of composite structural insulated panels. *Materials and Desig*n, *54C,* 1068-1082.

Tejchman, J. and Bobiński, J. (2012). *Continuous and discontinuous modelling of fracture in concrete using FEM*. Springer, Berlin-Heidelberg (eds. W. Wu and R. I. Borja).

www.sewaco.pl.

Xenos, D. and Grassl, P. (2016). Modelling the failure of reinforced concrete with non local and crack band approaches using the damage-plasticity model CDPM2. *Finite Elements in Analysis and Design,* 117-118, 11-20.

Xotta, G., Beizaee, S. and Willam, K.J. (2016). Bifurcation investigations of coupled damage-plasticity models for concrete materials. *Computer Methods in Applied Mechanics and Engineering*, 298, 428–452.

Appendix 1

In order to describe the concrete behaviour by an elasto-plastic constitutive model, two failure criteria were assumed. In a tensile regime, the Rankine criterion was used with the yield function f_1 using isotropic softening and associated flow rule and in a compressive regime, the Drucker-Prager yield surface f_2 with isotropic hardening/softening and non-associated flow rule was used

$$f_1(\sigma_i, \kappa_1) = max\{\sigma_1, \sigma_2, \sigma_3,\} - \sigma_t(\kappa_1) \leq 0 \qquad (A1)$$

$$f_2(\sigma_{ij}, \kappa_2) = q - p \times tan\,\varphi - c(\kappa_2) = q - p \times tan\,\varphi - \left(1 - \frac{1}{3}tan\,\varphi\right)\sigma_c(\kappa_2) \leq 0 \qquad (A2)$$

$$q = \sqrt{\frac{3}{2} s_{ij} s_{ij}}, \qquad p = -\frac{1}{3} \sigma_{kk} \tag{A3}$$

$$\tan \varphi = \frac{3\left(1 - r_{bc}^{\sigma}\right)}{1 - 2r_{bc}^{\sigma}} \tag{A4}$$

$$g_1 = f_1 \tag{A5}$$

$$g_2 = q - p \tan \psi \tag{A6}$$

where: σ_i - the principal stress (i=1, 2, 3), σ_t - the uniaxial tensile yield stress, κ_1 - the softening parameter equal to the maximum principal plastic strain ε_1^p, q - the Mises equivalent deviatoric stress, p - the mean stress, φ - the internal friction angle in the meridional stress plane (p–q plane), c - the cohesion related to uniaxial compression strength, s_{ij} - the deviator of the stress tensor σ_{ij}, ($s_{ij}=\sigma_{ij}+\delta_{ij}p$) σ_c - the uniaxial compression yield stress, κ_2 - the hardening/softening parameter corresponding to the plastic vertical normal strain during uniaxial compression, g_i – flow potential function, r_{bc}^{σ} - the ratio between the biaxial compressive strength and uniaxial compressive strength ($r_{bc}^{\sigma}{\approx}1.2$) and ψ - the dilatancy angle ($\psi{\neq}\varphi$). The last term in Equation (A3) results from the yield condition $q{-}p{\times}\tan\varphi{-}c{=}0$ for uniaxial compression with $q{=}\sigma_c$ and $p{=}1/3\sigma_c$.

Appendix 2

The coupled elasto-plastic-damage model for concrete (Marzec & Tejchman 2012, Marzec et al., 2013) combines elasto-plasticity with a scalar isotropic damage assuming a strain equivalence hypothesis according to Pamin & de Borst (1999). The elasto-plasticity was defined in terms of effective stresses according to

$$\sigma_{ij}^{eff} = C_{ijkl}^e \varepsilon_{kl} \tag{A7}$$

In an elasto-plastic regime, a linear isotropic Drucker-Prager criterion with a non-associated flow rule in compression and a Rankine criterion with an associated flow rule in tension (Appendix 1) defined by the effective stresses were used. The material degradation was calculated within isotropic damage mechanics, independently in tension and compression using one equivalent strain measure $\tilde{\varepsilon}$ (Mazars & Pijaudier-Cabot 1996) (ε_i - principal strains)

$$\tilde{\varepsilon} = \sqrt{\sum_i \langle \varepsilon_i \rangle^2} \tag{A8}$$

The equivalent strain measure $\tilde{\varepsilon}$ was defined in terms of elastic strains. The stress-strain relationship was represented by following formula

$$\sigma_{ij} = \left(1 - D\right)\sigma_{ij}^{eff} \tag{A9}$$

with the term '1-D' defined as:

19

$$(1 - D) = (1 - s_c D_t)(1 - s_t D_c) \tag{A10}$$

wherein

$$D_t = 1 - \frac{\kappa_0}{\kappa}(1 - \alpha + \alpha e^{-\beta(\kappa - \kappa_0)}) \tag{A11}$$

$$D_c = 1 - \left(1 - \frac{\kappa_0}{\kappa}\right)\left(0.01 \frac{\kappa_0}{\kappa}\right)^{\eta_1} - \left(\frac{\kappa_0}{\kappa}\right)^{\eta_2} e^{-\delta(\kappa - \kappa_0)} \tag{A12}$$

$$s_t = 1 - a_t w\left(\sigma_{ij}^{eff}\right) \quad \text{and} \quad s_c = 1 - a_c \left(1 - w\left(\sigma_{ij}^{eff}\right)\right) \tag{A13}$$

$$w\left(\sigma_{ij}^{eff}\right) = \begin{cases} 0 & \text{if } \sigma_{ij}^{eff} = 0 \\ \dfrac{\sum \left\langle \sigma_i^{eff} \right\rangle}{\sum \left| \sigma_i^{eff} \right|} & \text{otherwise} \end{cases} \tag{A14}$$

where D_t and D_c are damage parameters describe the damage evolution under tension (Peerlings et al., 1998) and compression (Geer 1997) with the material constants: α, β, η_1, η_2, δ, a_t and a_c are the scale factors and $w\left(\sigma_{ij}^{eff}\right)$ denotes the stress weight function (Lee &Fenves 1998). The bracket in Equation (A14) is defined as $\langle x \rangle = (x + |x|)/2$.

LIST OF FIGURES

a)

b)
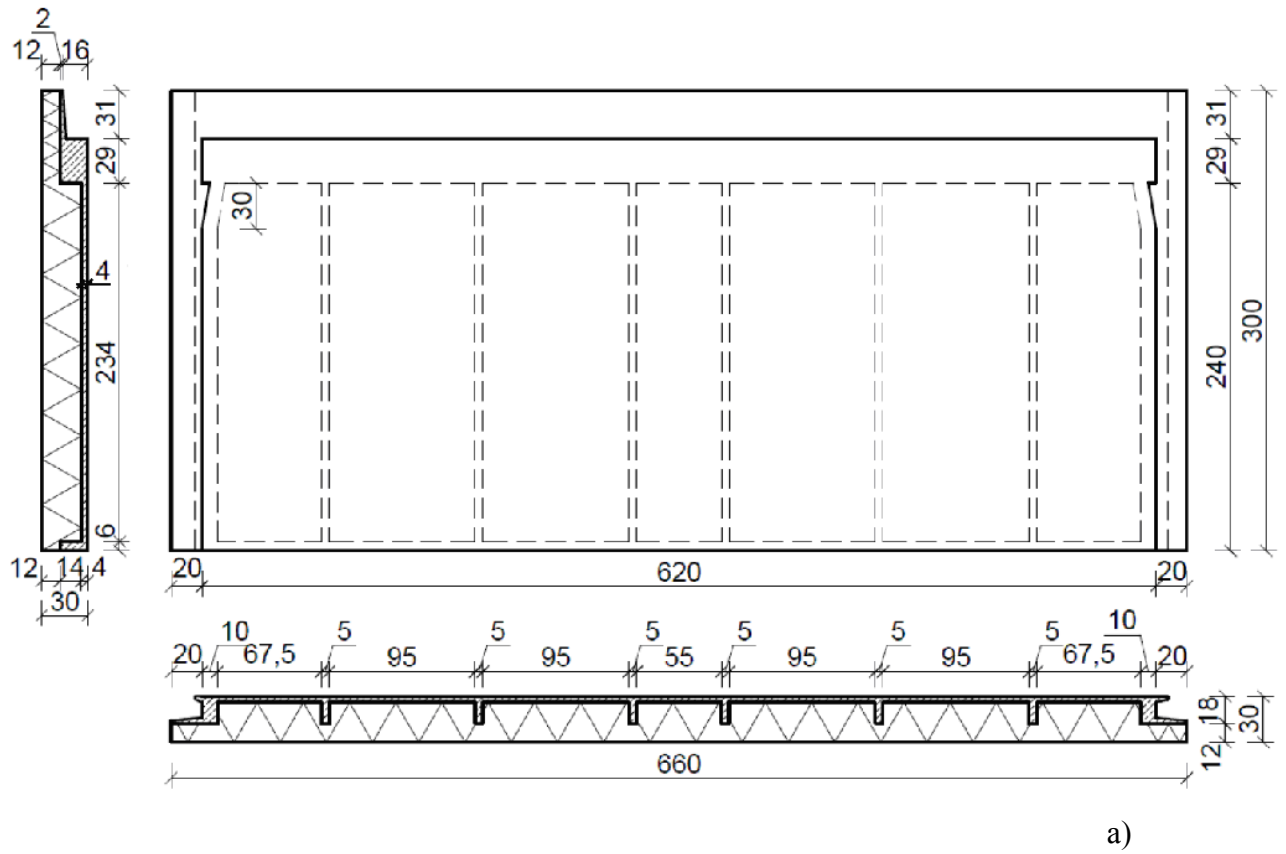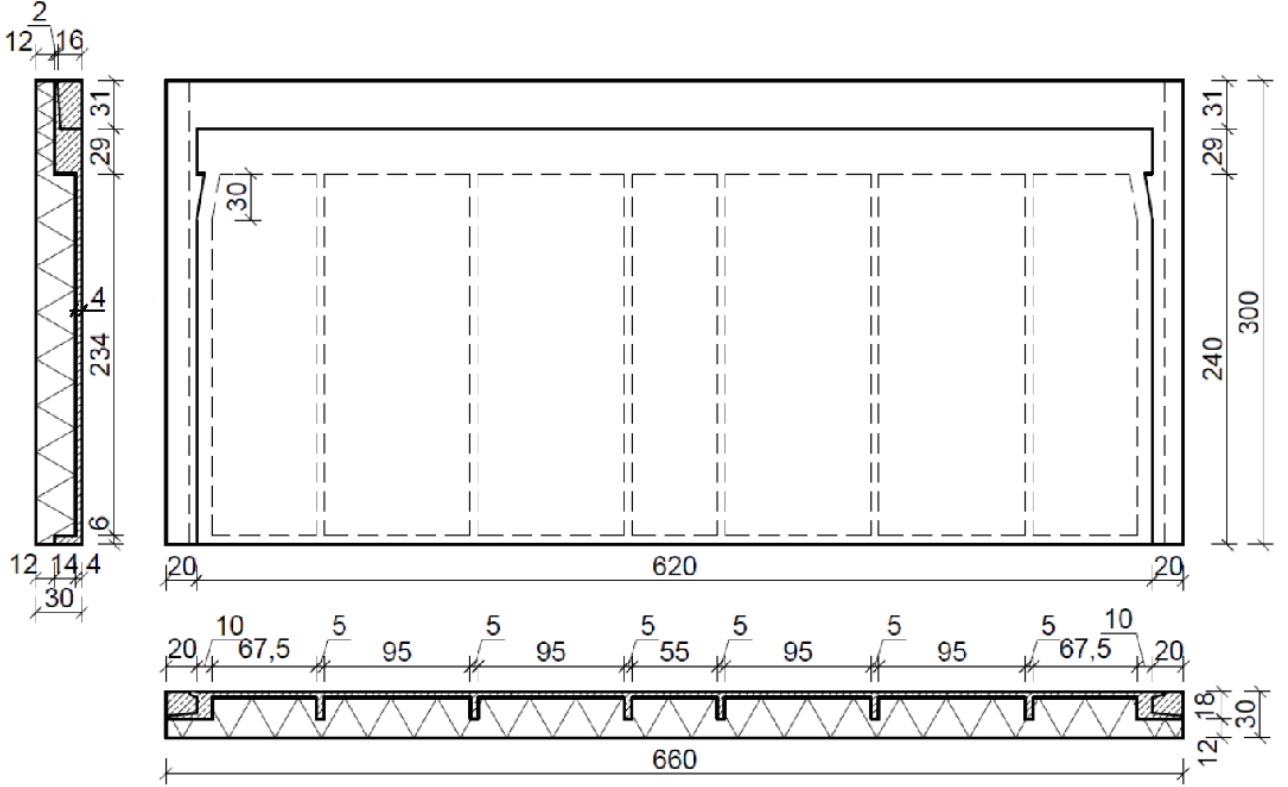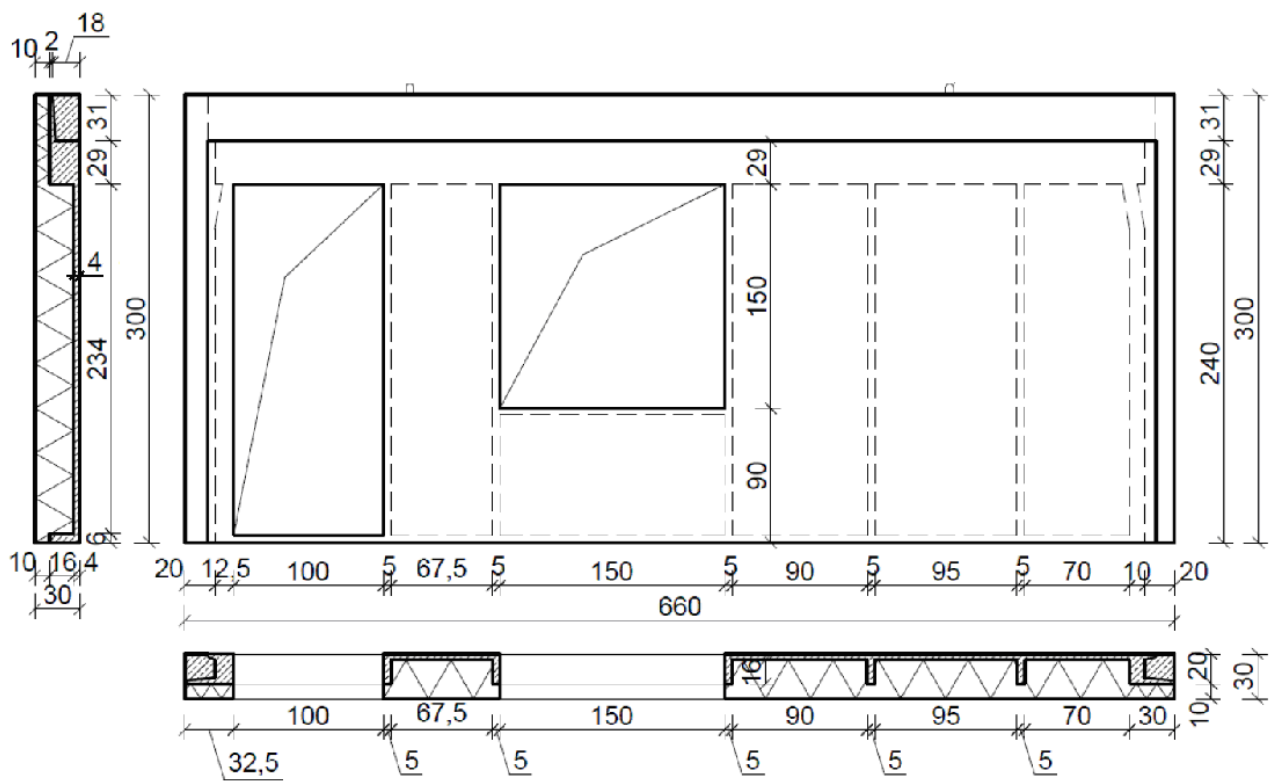
Fig.1: Geometry of prefabricated composite wall panels: a) full panel '1' without monolithic frame, b) full panel '2' surrounded by monolithic frame and c) a) panel '3' including window and door holes surrounded by monolithic frame

FIGURE 1

A

1x Ø10

3x Ø14

|←30→|←30→|←30→|←30→|←30→|←30→|←30→|←30→|←30→|←30→|←30→|←30→|←30→|←30→|←30→|←30→|←30→|←30→|←30→|←30→|←30→|

10   21Ø10   10

41x15cm=615cm

2,5   42Ø6   2,5

A

1x Ø10 L=656 cm

3x Ø14 L=656 cm

Cross section A-A

18

31

29

Ø10
Ø6
Ø10

Ø14

Reinforcement

8,5

42Ø6

3

54

25

13,5

56

12Ø10

a)

Steel mesh G188 O6_15x15cm   α – α

Steel mesh G188 O6_15x15cm   β— β

Steel mesh G188 O6_15x15cm   γ— γ

Steel mesh G188 O6_15x15cm
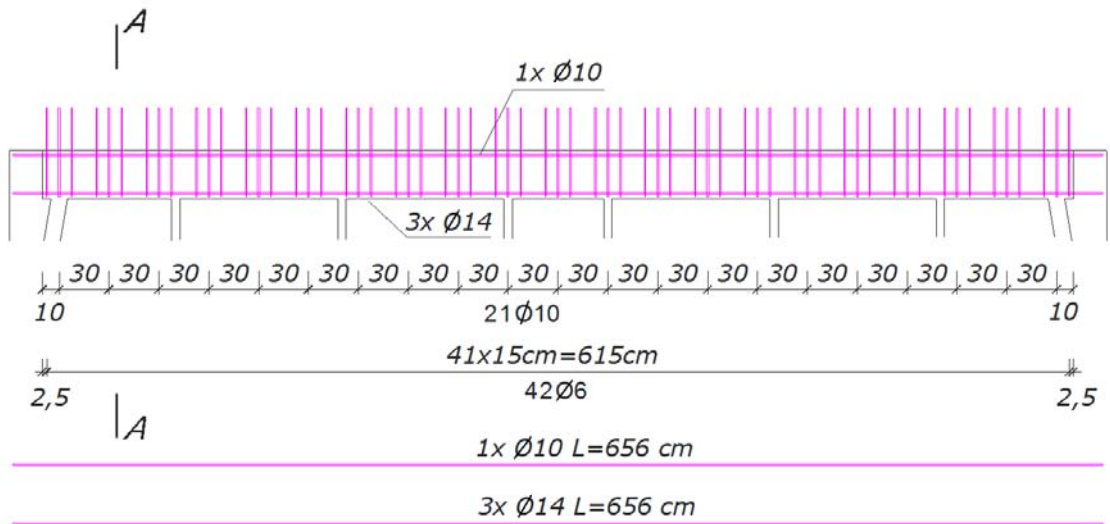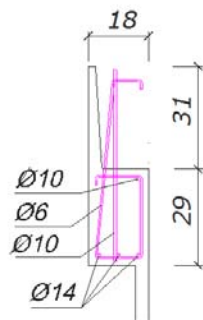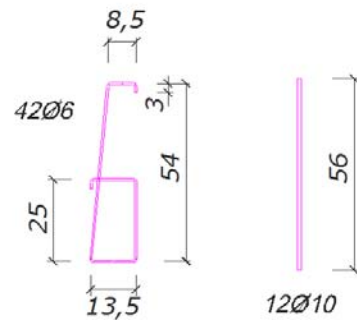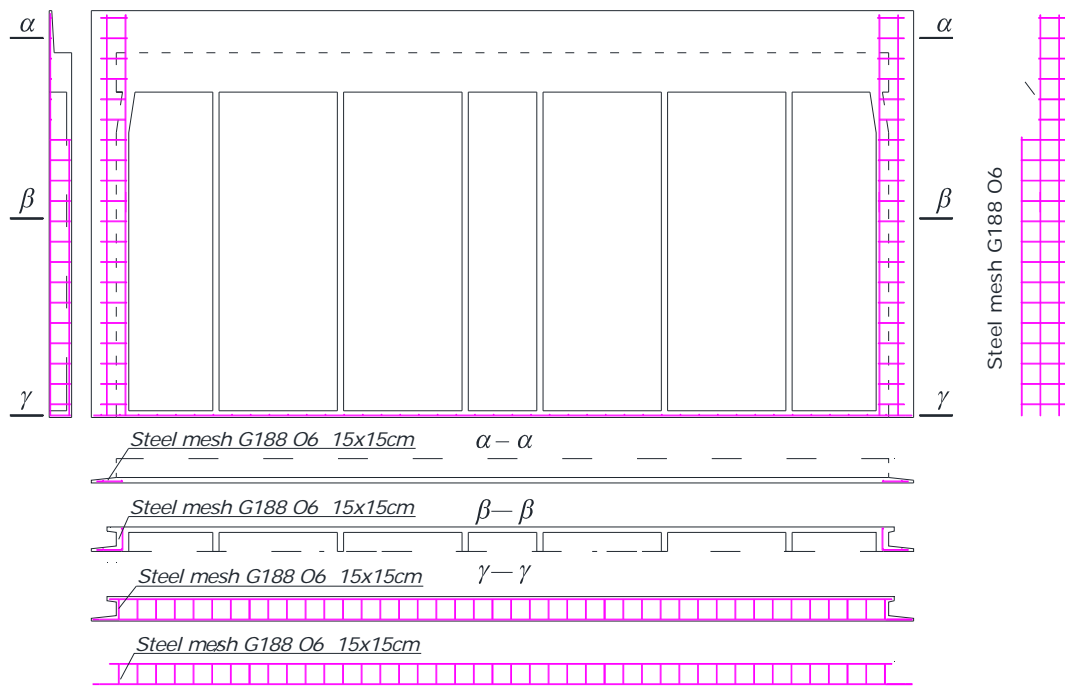
b)

Fig.2: Composite wall panel '1' without monolithic frame: a) top reinforcement, b) side and bottom reinforcement

FIGURE 2
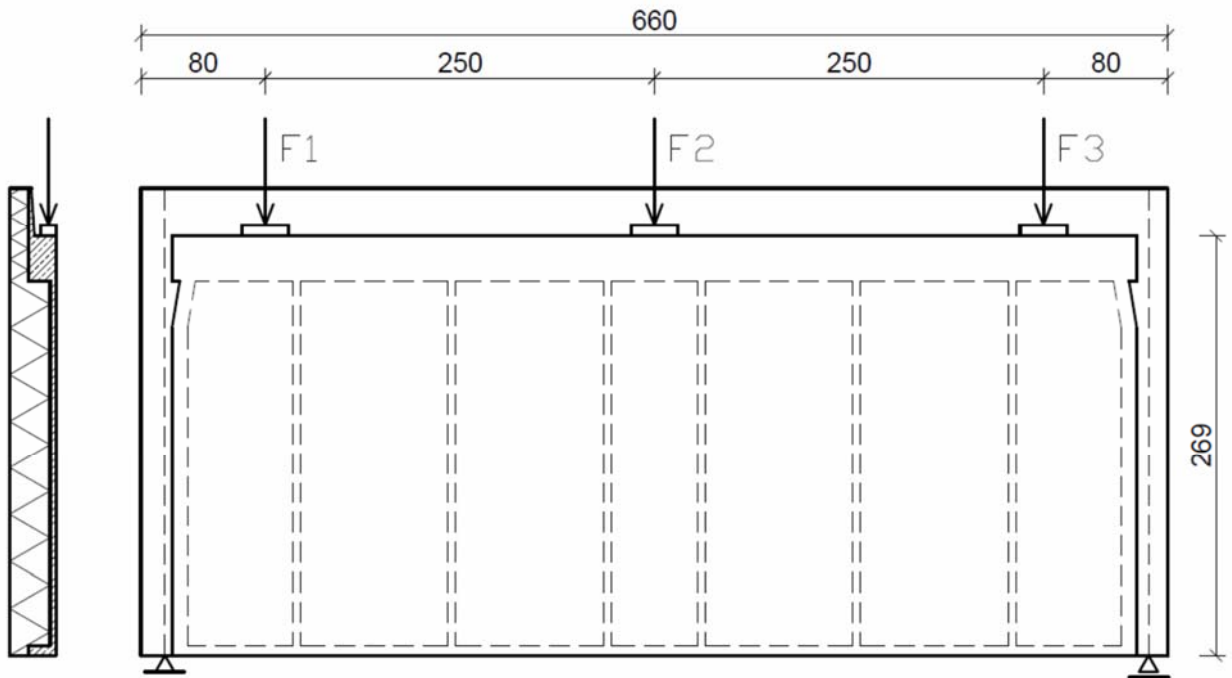
Fig.3: Loading system of composite wall panel '1' without monolithic frame during bending (units in [cm])

FIGURE 3
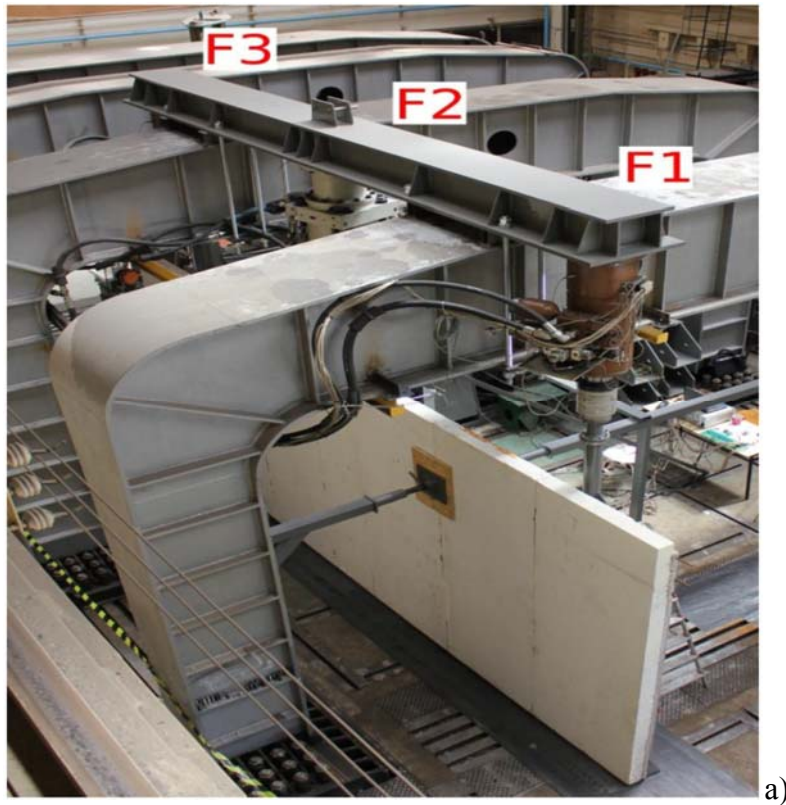
Fig.4: Experimental set-up for composite wall panel '1' without monolithic frame: a) top view and b) view on steel plates on rubber pads (*F1-F3* - vertical forces)

FIGURE 4

A)

B)
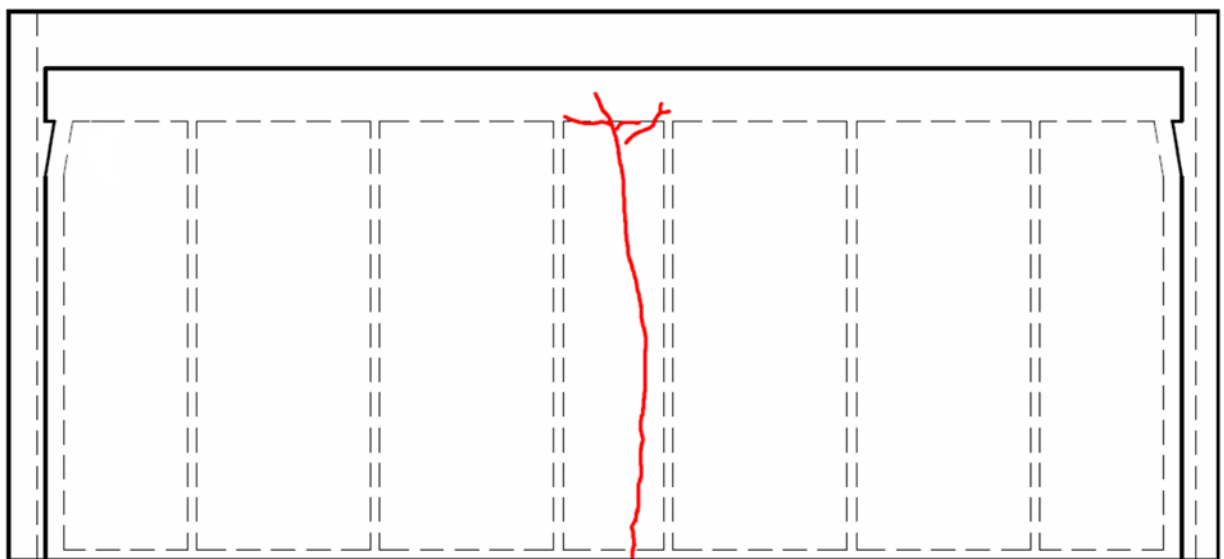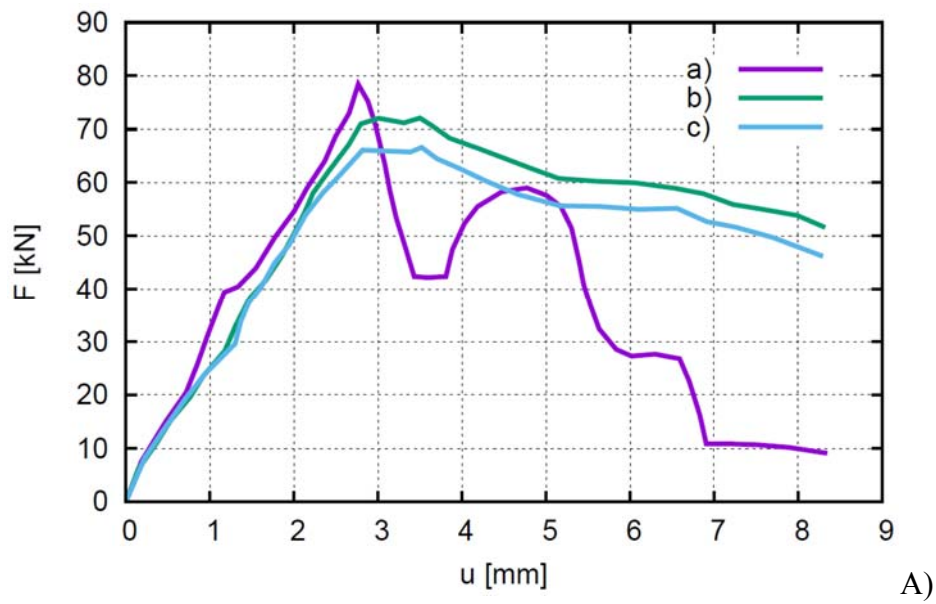
Fig.5: Composite wall panel '1' without monolithic frame: A) evolution of vertical forces F_1 (a), F_2 (b) and F_3 (c) along frame top against mid-slab deflection u and B) crack location (in red) for maximum total vertical force $F_{max}=F_1+F_2+F_3=221.4$ kN ($u=2.86$ mm)

FIGURE 5
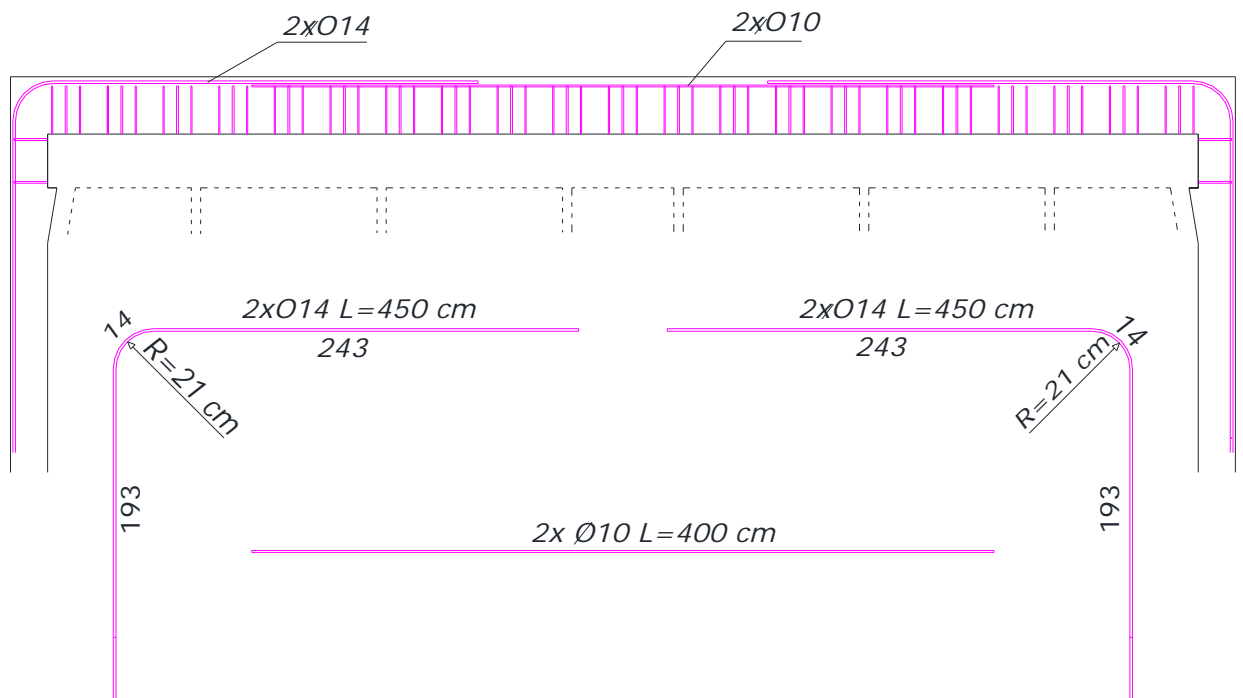
Fig.6: Composite wall panel '2' with monolithic frame: frame reinforcement

FIGURE 6
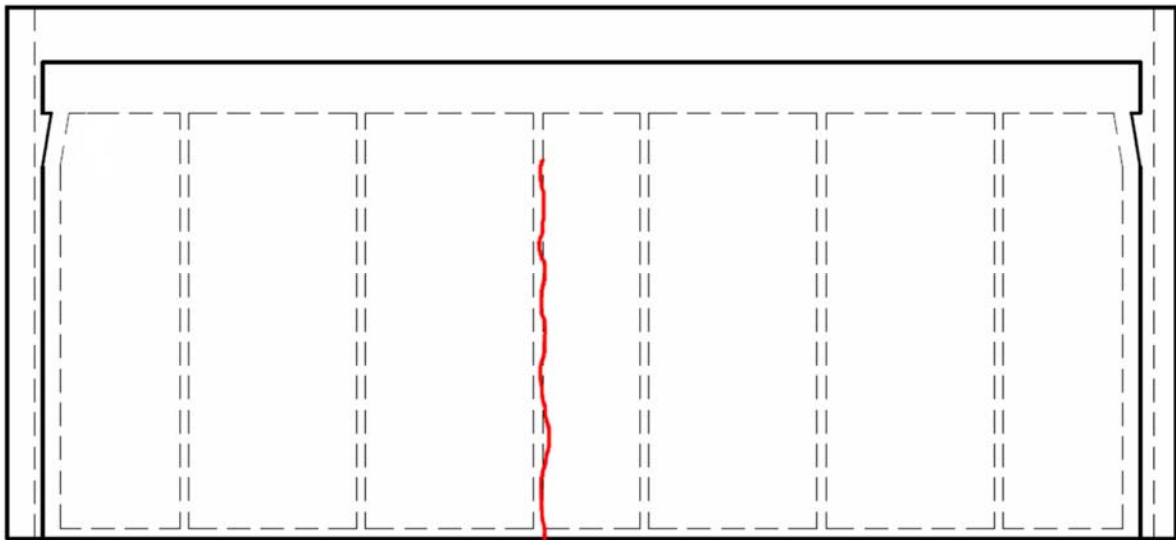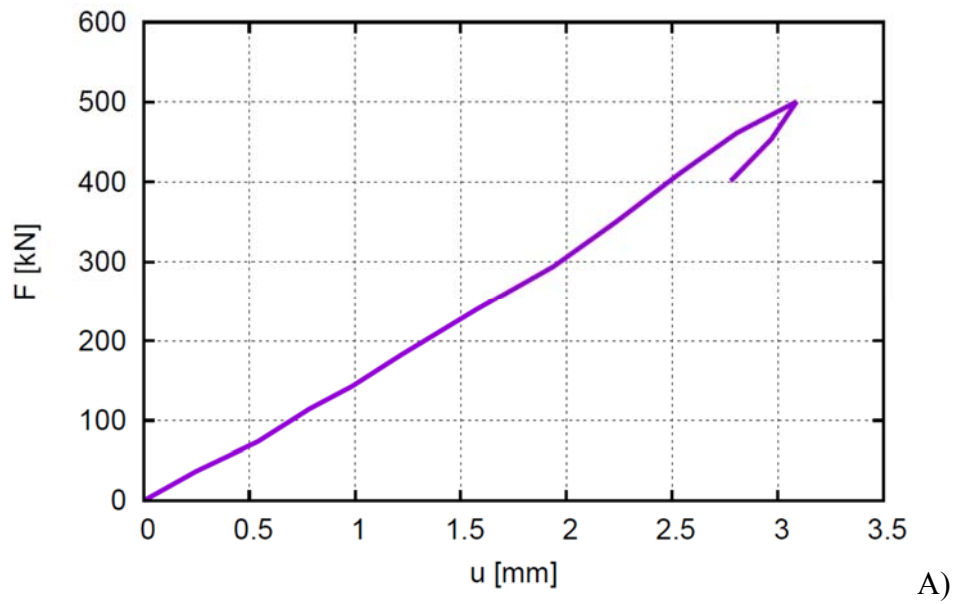
Fig.7: Composite wall panel '2' surrounded by monolithic frame: A) evolution of vertical force F against mid-slab deflection u and B) crack pattern (in red) for F_{max} (u=3.1 mm)

FIGURE 7

Fig.8: Composite wall panel '2': local damage of concrete under vertical force

FIGURE 8

Nr 4 2Φ12 L=450cm

Nr 4 2Φ12 L=450cm

243

243

R21

R21

193

193

Nr 3 2Φ10 L=400cm

Nr 2 1Φ10 L=655cm

A

Nr 1 2Φ10 L=655cm

Nr 4 2Φ12

Nr 3 2Φ10

Nr 4 2Φ12

23

23

A

Nr 1 2Φ10

Nr 2 Φ10

B

B

Nr 5 4Φ10 L=280cm

9 x 30 = 270 cm

Nr 7 10Φ6

20 x 30 = 600 cm
Nr 9 21Φ10

20 x 30 = 600 cm
Nr 8 21Φ6

9 x 30 = 270 cm

Nr 7 10Φ6

Nr 5 4Φ10 L=280cm

Nr 5 4Φ12

Nr 5 4xΦ12

Q188

Nr 6 2Φ10

Nr 6 2Φ10 L=615cm

steel mesh Q188

Nr 4 2Φ12

Nr 3 2Φ10

Nr 2 Φ10

Nr 5 4Φ10

A–A

Nr 1 2Φ10

B–B

Fig.9: Reinforcement of composite wall panel '3' surrounded by monolithic frame

FIGURE 9
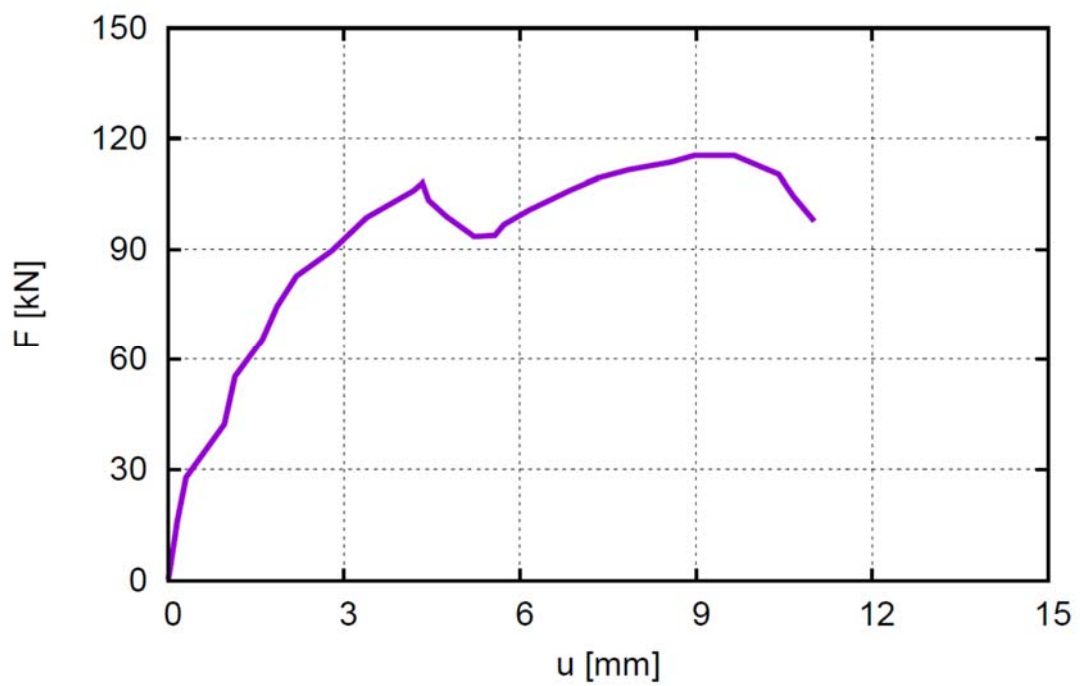
Fig.10: Composite wall panel '3' with monolithic frame: evolution of vertical force *F* against mid-slab deflection *u*

FIGURE 10
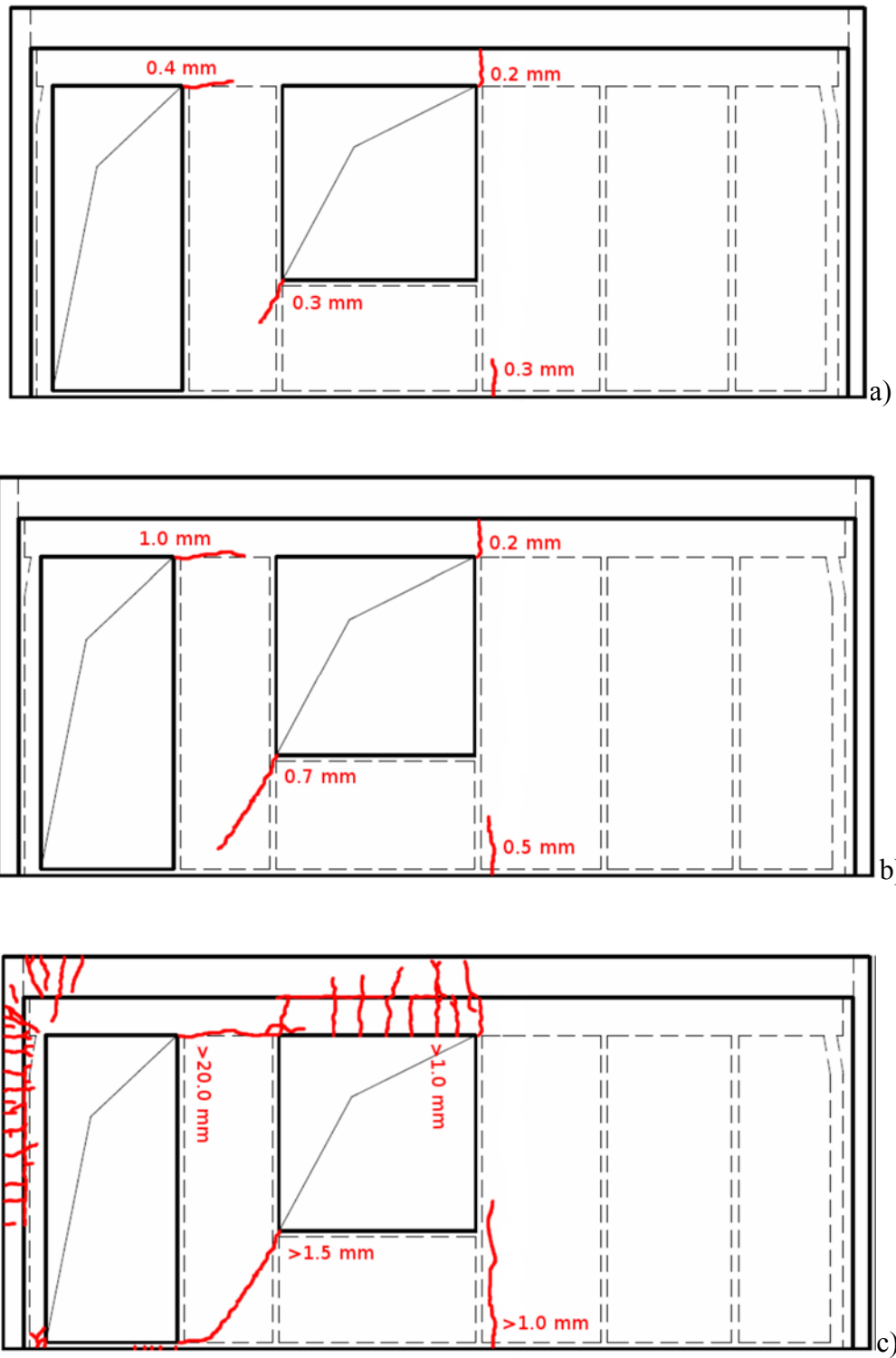
Fig.11: Composite wall panel '3' with monolithic frame: crack evolution (in red) for different vertical force F: a) F=70 kN (u=1.83 mm), b) F=80 kN (u=2.19 mm) and c) F_{max}=118 kN (u=9.2 mm)

FIGURE 11

a)

b)

c)

35
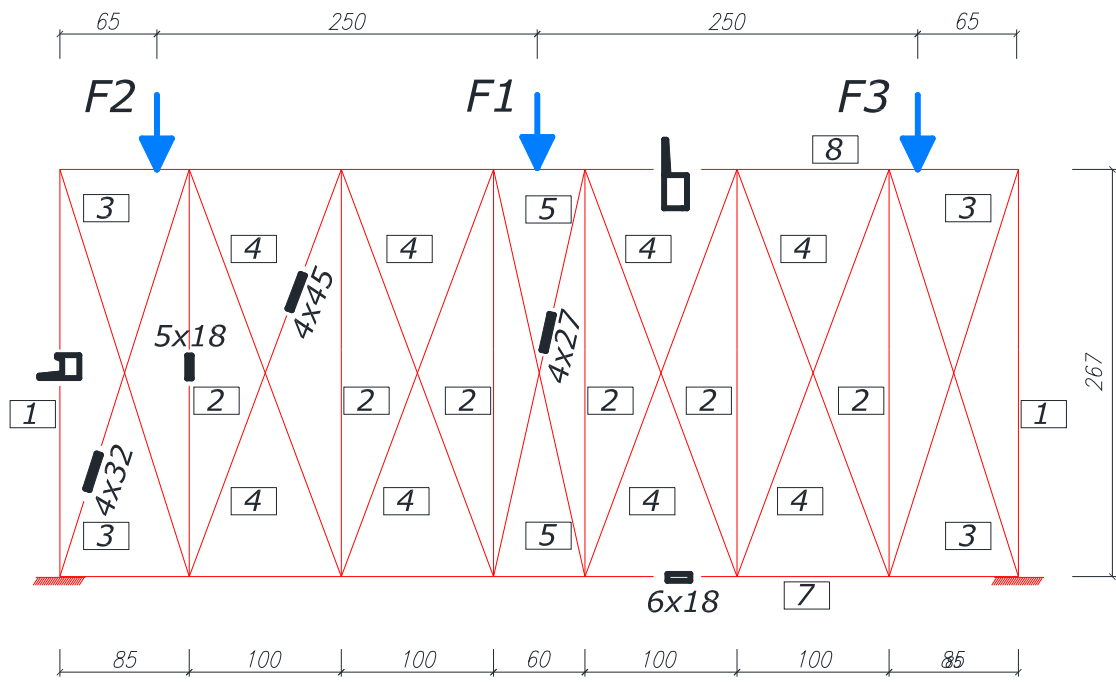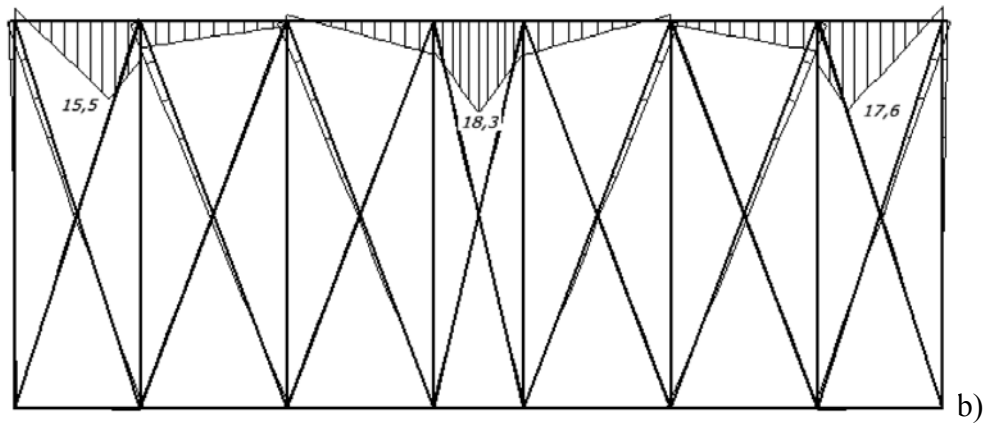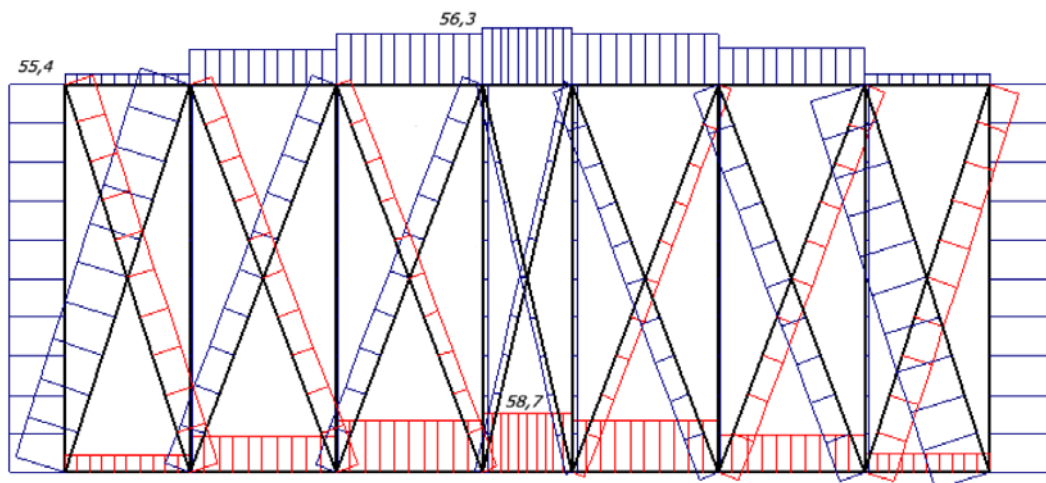
Fig.12: TWM results (panel '1') for maximum total vertical force (F_1=80 kN, F_2=65 kN, F_3=75 kN): a) static system, b) bending moments and c) normal forces (red colour - tension, blue colour - compression)

FIGURE 12
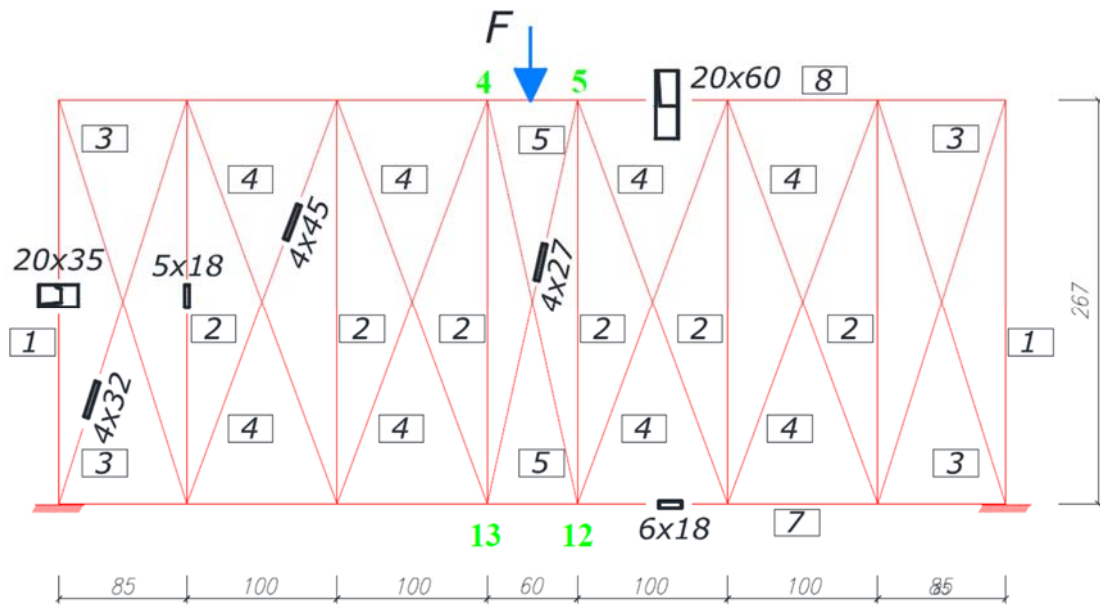
a)
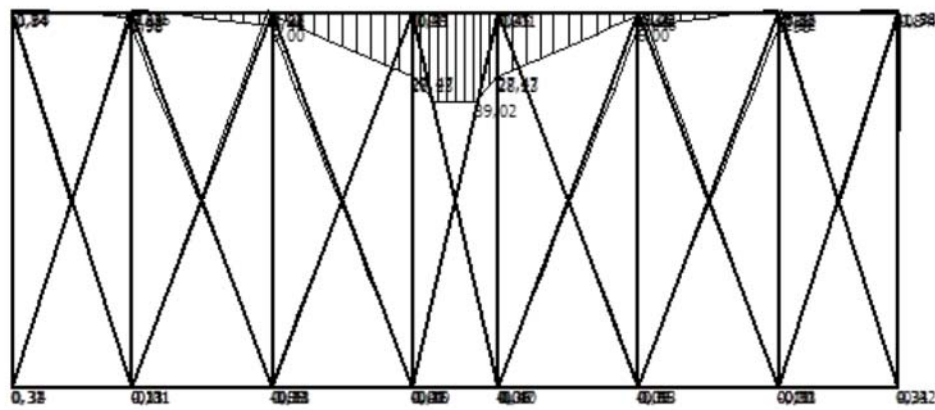
b)
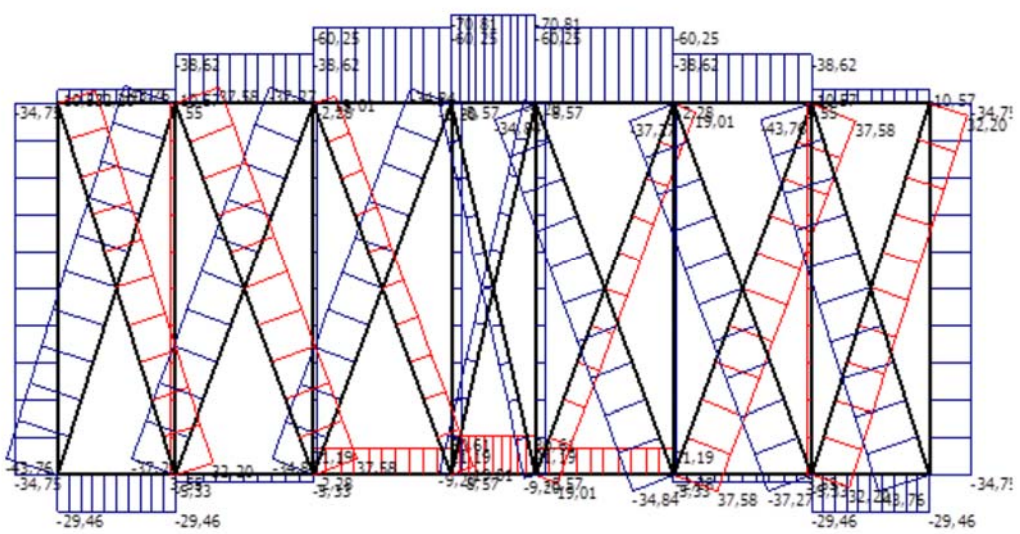
c)

Fig.13: TWM results (panel '2') for cracking vertical force (F=134 kN): a) static system, b) bending moments and c) normal forces

FIGURE 13
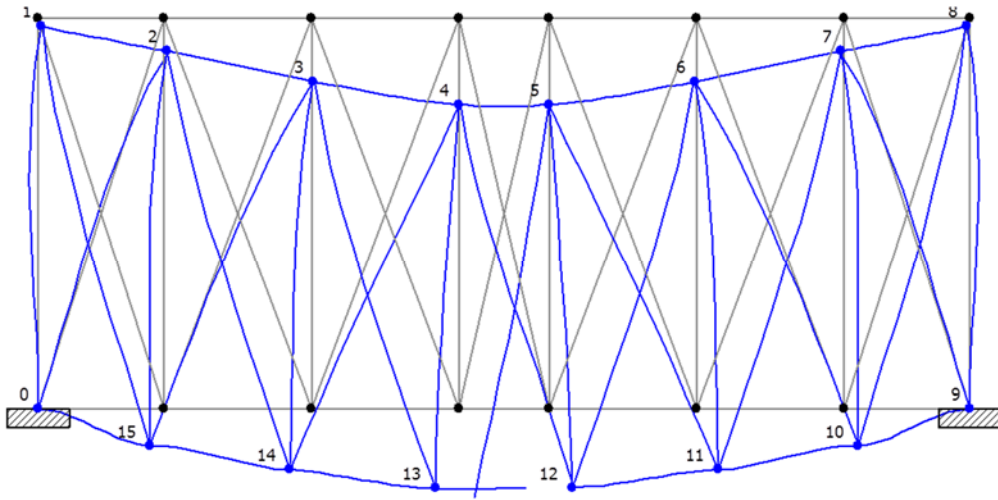
a)
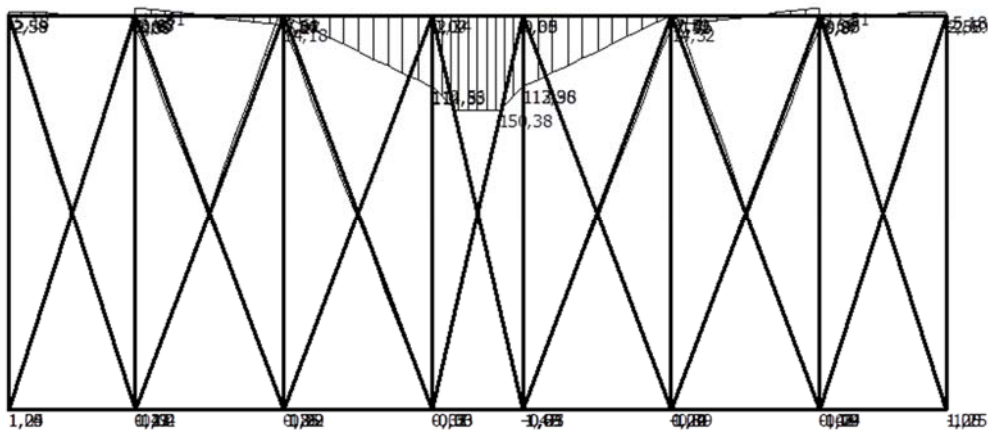
b)
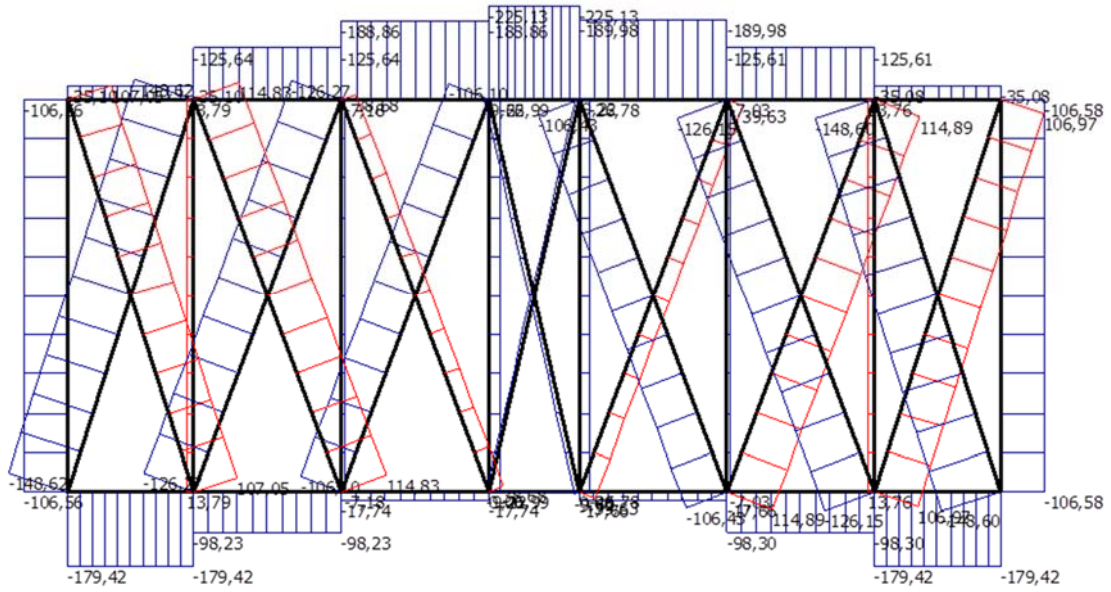
c)

Fig.14: TWM results (panel '2') for failure vertical force (*F*=501 kN): a) static system, b) bending moments and c) normal forces

FIGURE 14
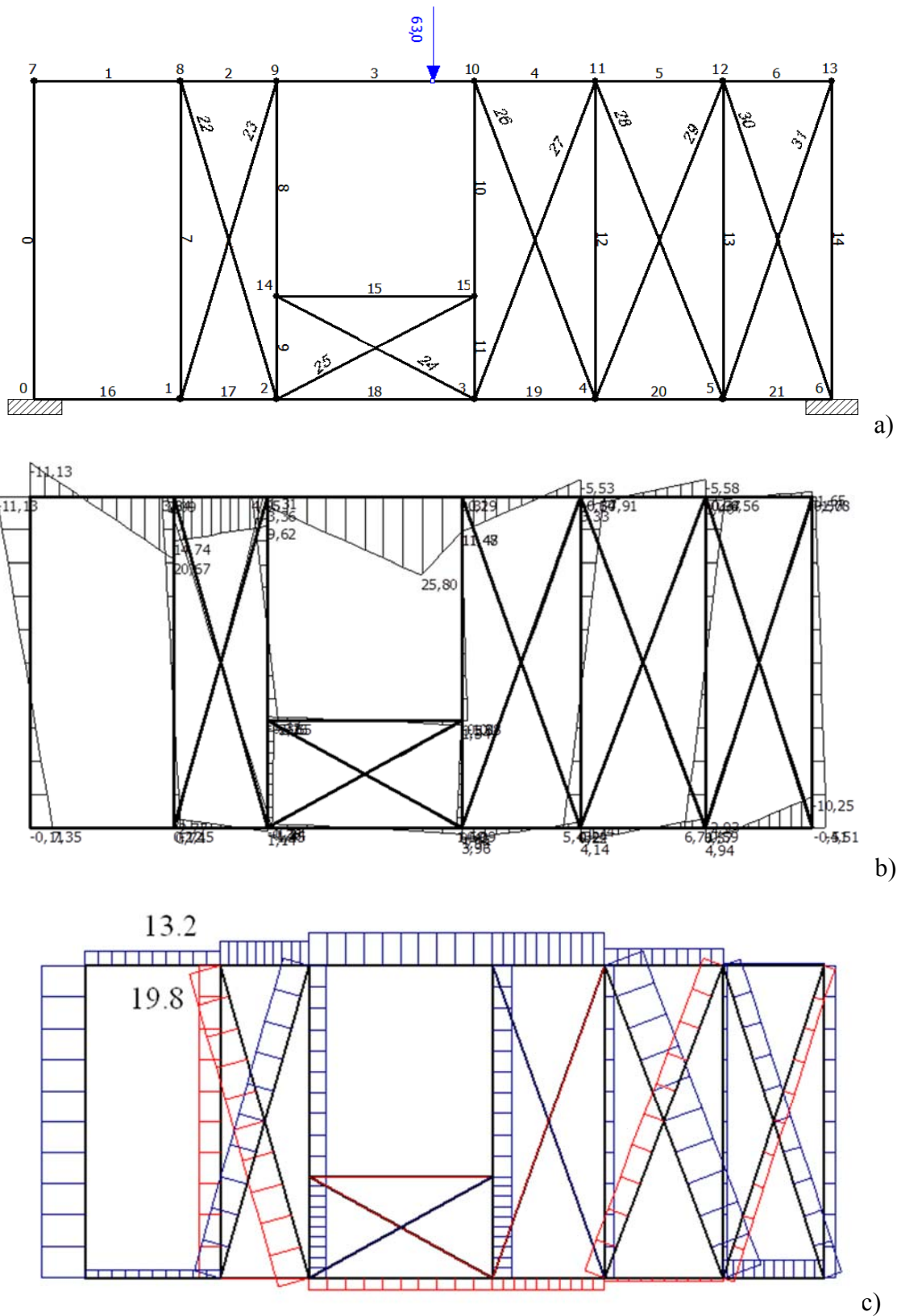
Fig.15: TWM (panel '3') before cracking (*F*=63 kN): a) static system, b) bending moments and c) normal forces

FIGURE 15

41
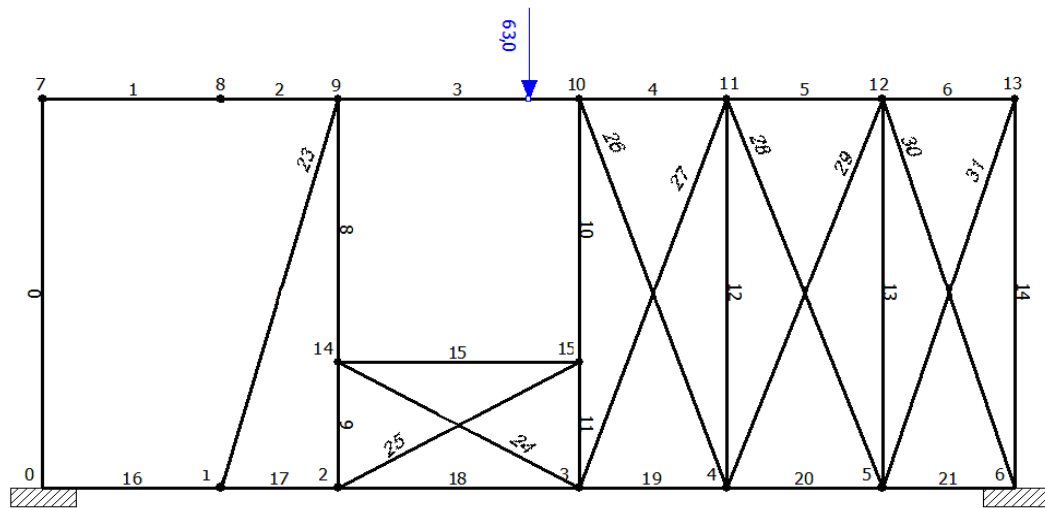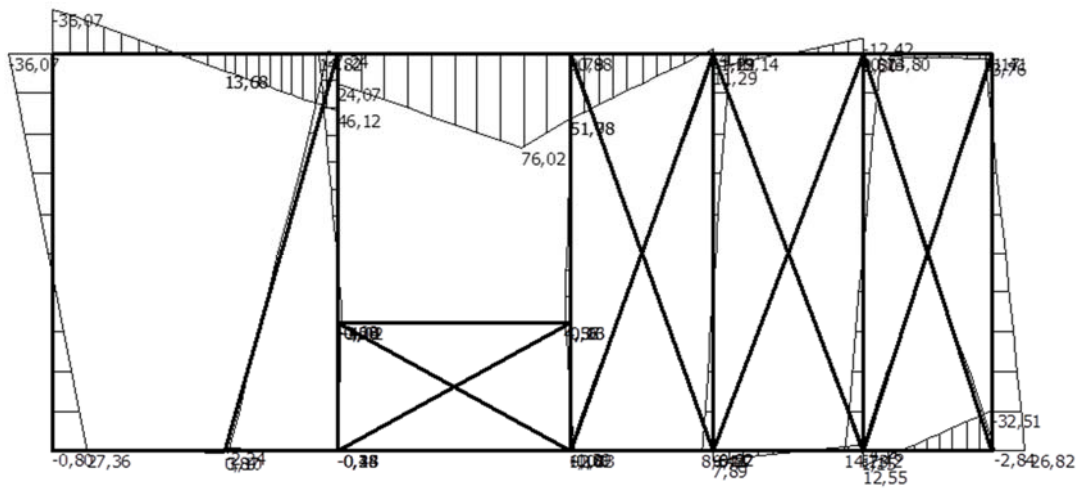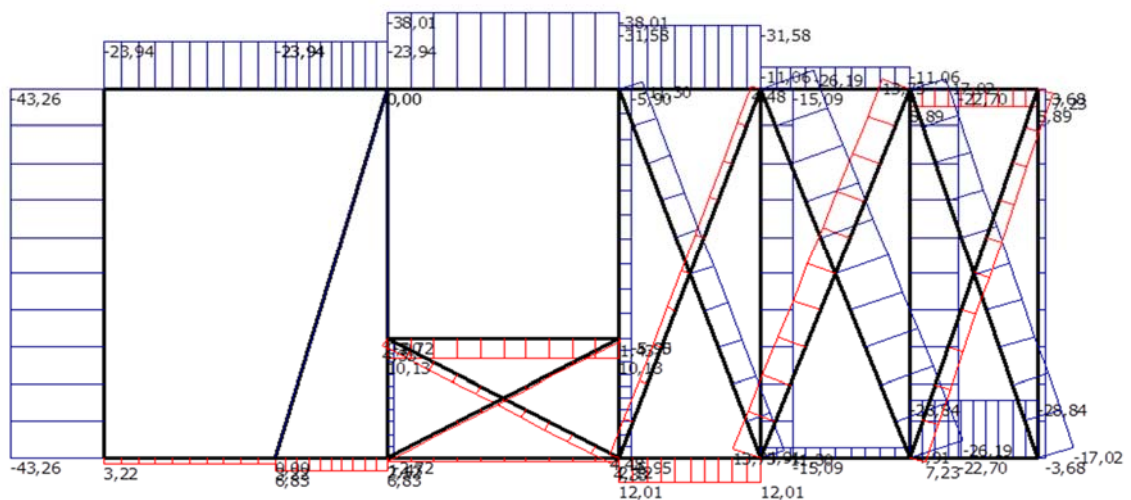
Rys.16: TWM results (panel '3') for vertical failure force (*F*=118 kN): a) static system, b) bending moments and c) normal forces

FIGURE 16
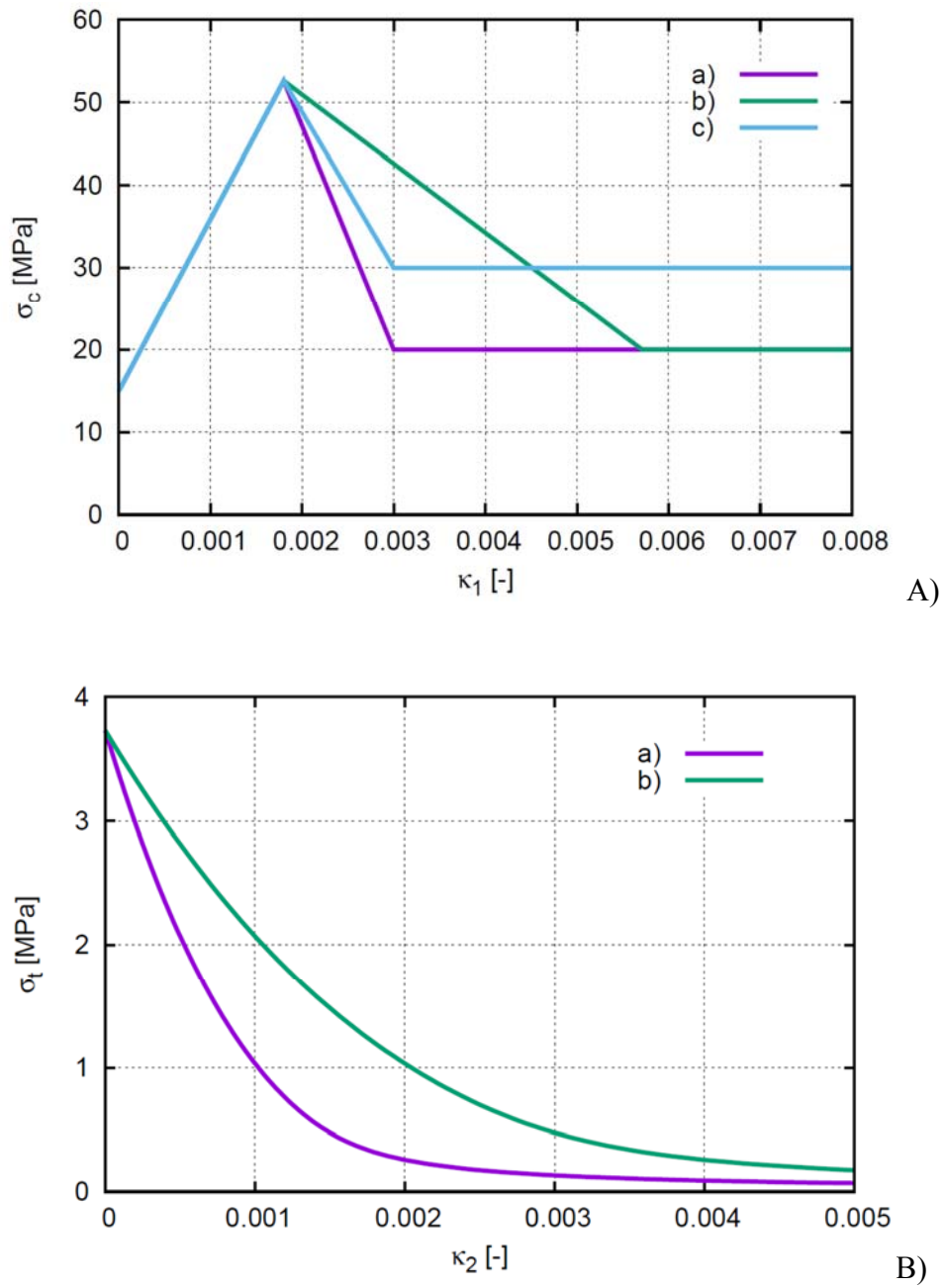
Fig.17: Different curves assumed in enhanced elasto-pasticity: A) 3 linear hardening/softening curves $\sigma_c = f(\kappa_1)$ in compressive regime and B) 2 non-linear softening curves $\sigma_t = f(\kappa_2)$ in tensile regime (σ_c - compressive stress, σ_t - tensile stress, κ_i - hardening/softening parameter)

FIGURE 17
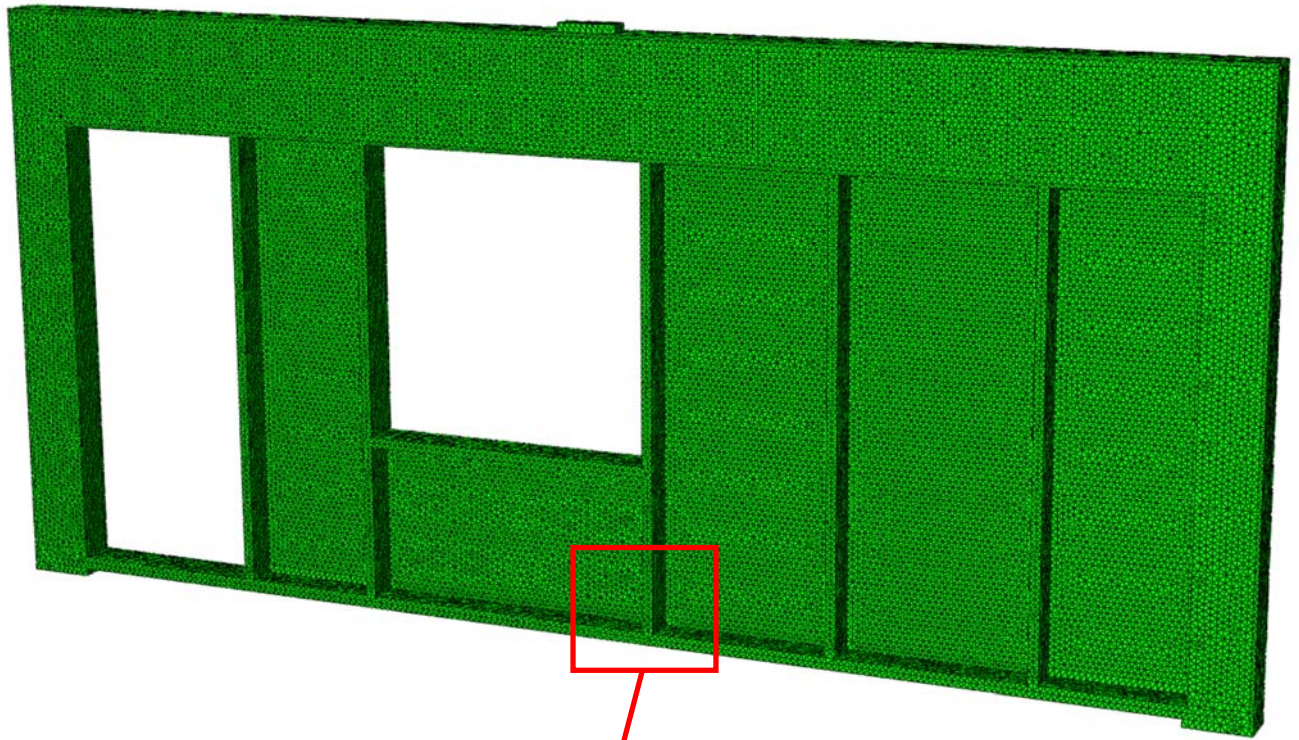
a)
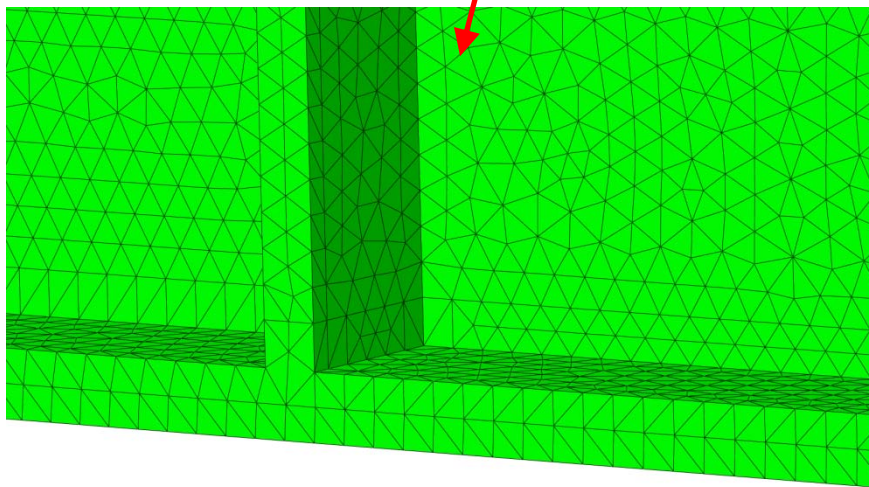
b)

Fig.18: FE mesh for composite wall panel '3' (without EPS): a) entire mesh and b) zoom on mesh

FIGURE 18

44

a)

b)

45
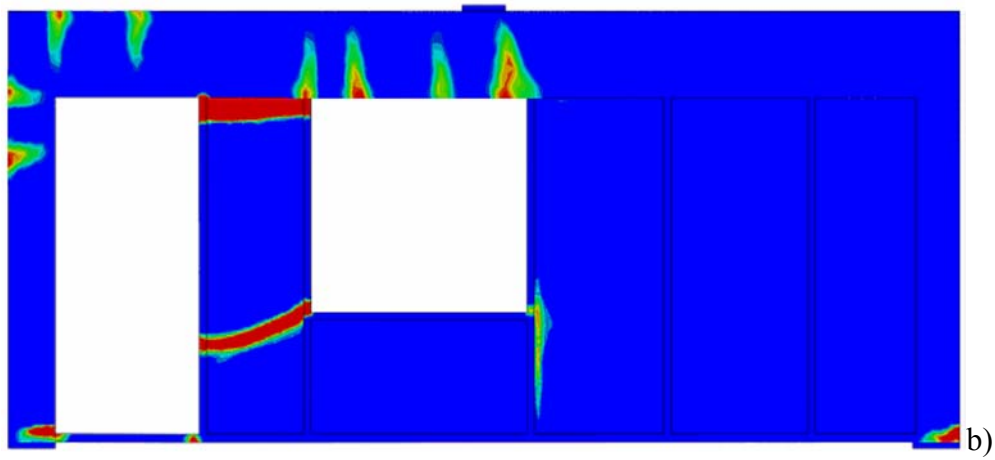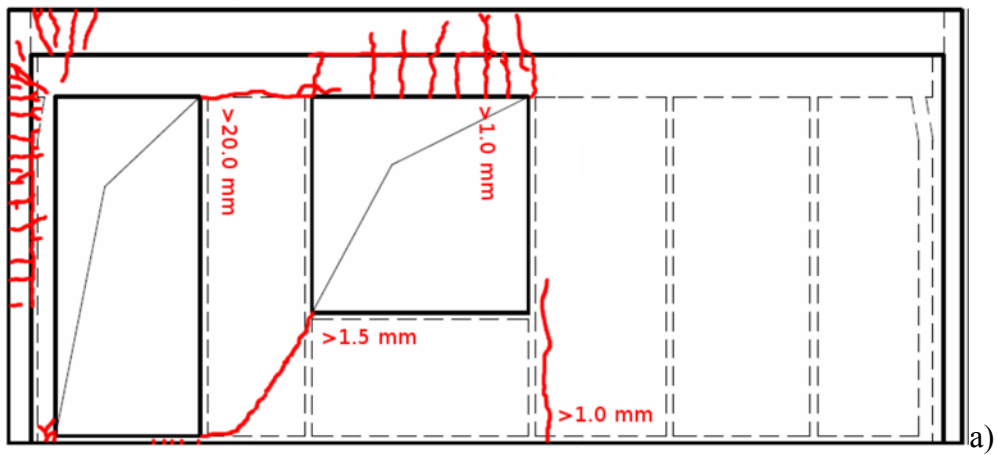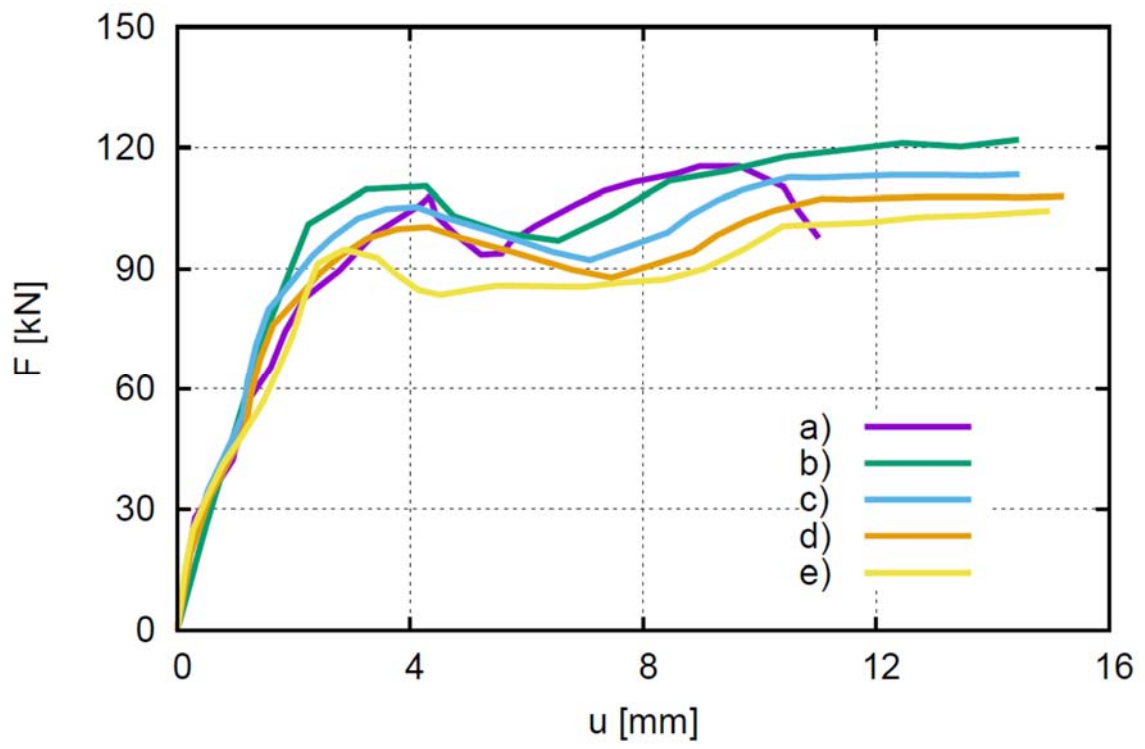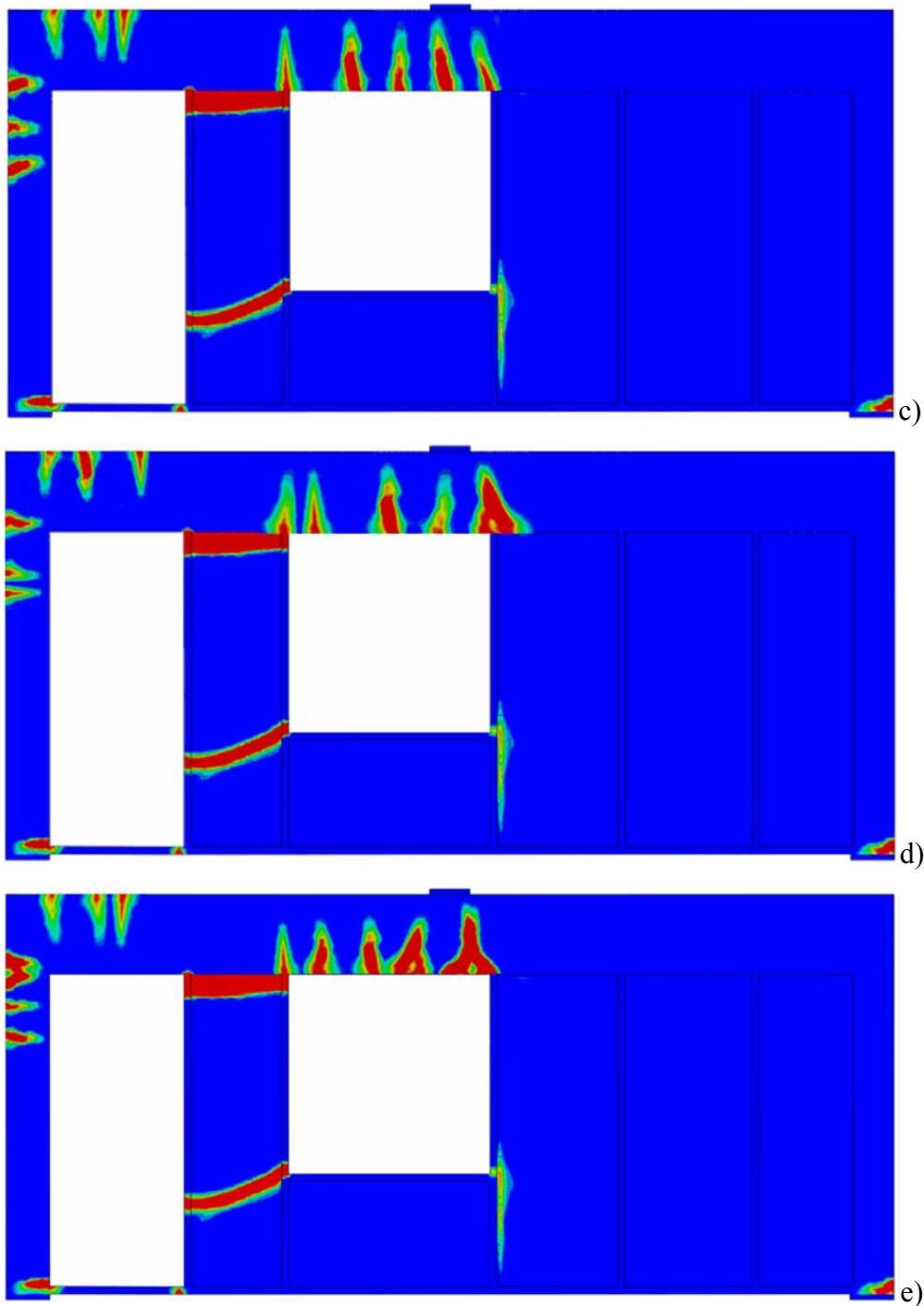
Fig.19: Vertical force-deflection curves $F=f(u)$ and distribution of non-local tensile softening parameter κ_2 (u=11 mm) for composite wall panel from FE analyses within enhanced elasto-plasticity as compared to experiment (compressive fracture energy G_c=2750 N/m - curve 'a' of Fig.17A), tensile fracture energy G_f=200 N/m (curve 'a' of Fig.17B) and characteristic length of micro-structure l_c=5 mm): a) experiment (Fig.11c), b) FEM (perfect bond), c) FEM (bond-slip with u_0=0.03 mm (Eq.4) and, d) FEM (bond-slip with u_0=0.06 mm) and e) FEM (bond-slip with u_0=1.0 mm)

46

FIGURE 19
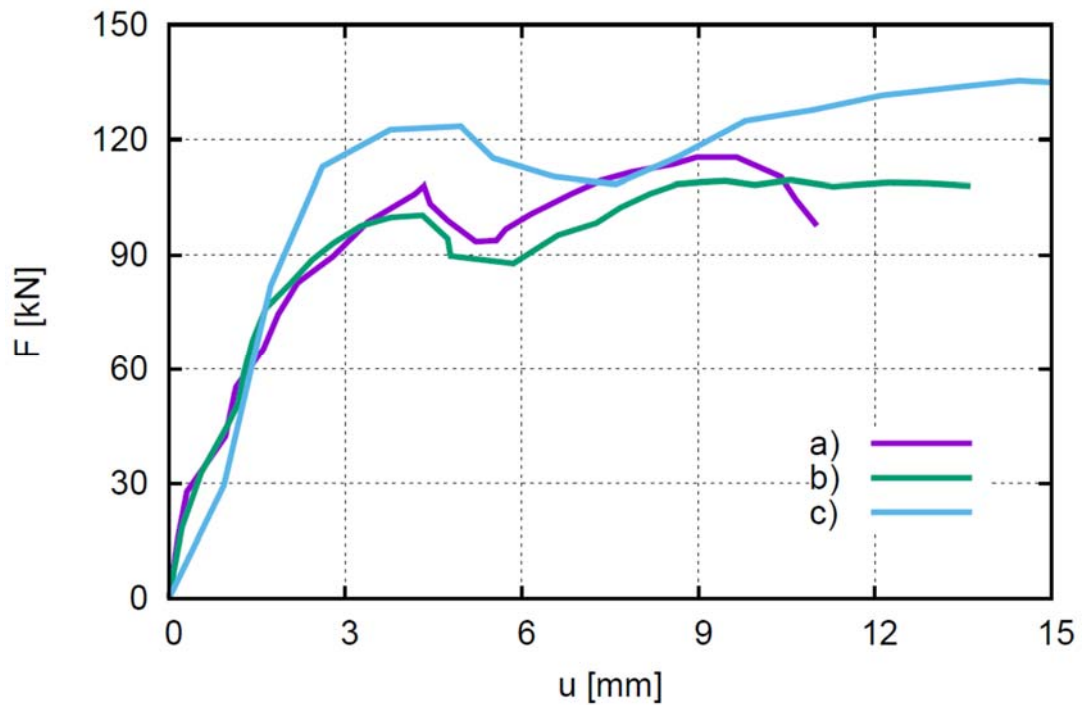
Fig.20: Vertical force-deflection curves $F=f(u)$ composite wall panel from FE analyses within enhanced elasto-plasticity with different tensile fracture energy G_f (compressive fracture energy G_c=3250 N/m (curve 'b' of Fig.17A), bond slip with u_0=0.03 mm and characteristic length of micro-structure l_c=5 mm): a) experimental result (Fig.10), b) FEM with G_f=200 N/m (curve 'a' of Fig.17B) and c) FEM with G_f=400 N/m (curve 'b' of Fig.17B)
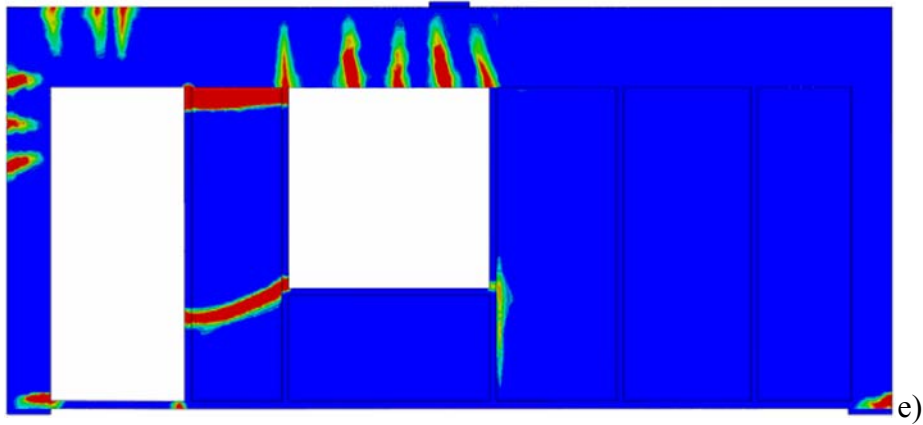
FIGURE 20

a)

b)

c)

d)

50

e)
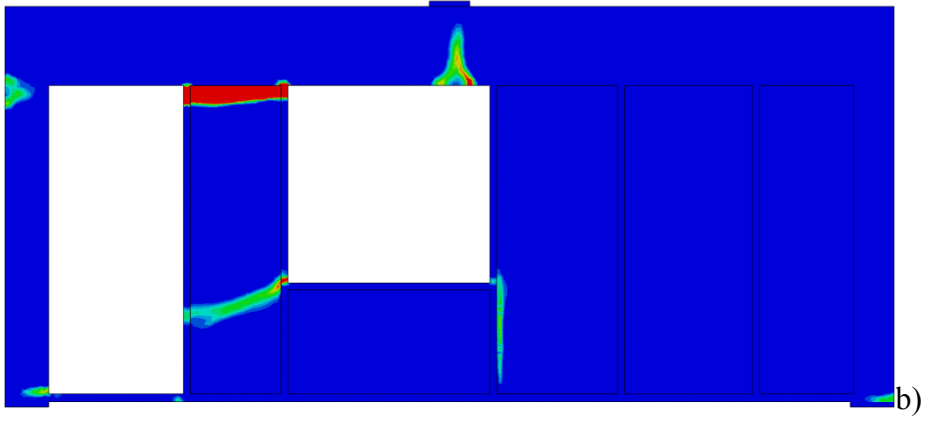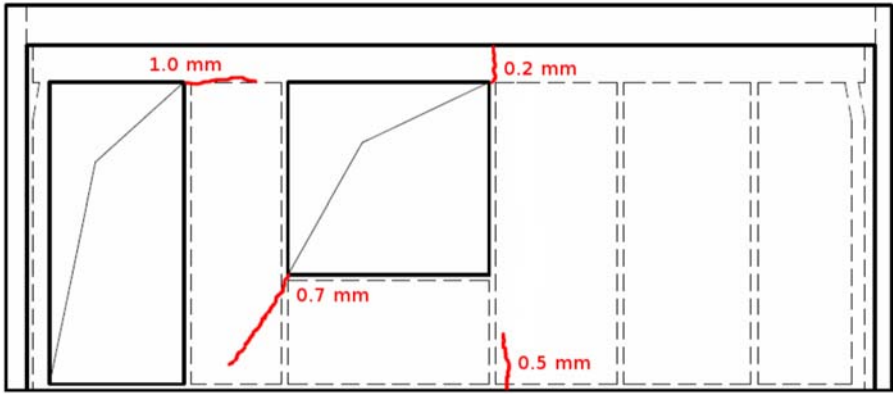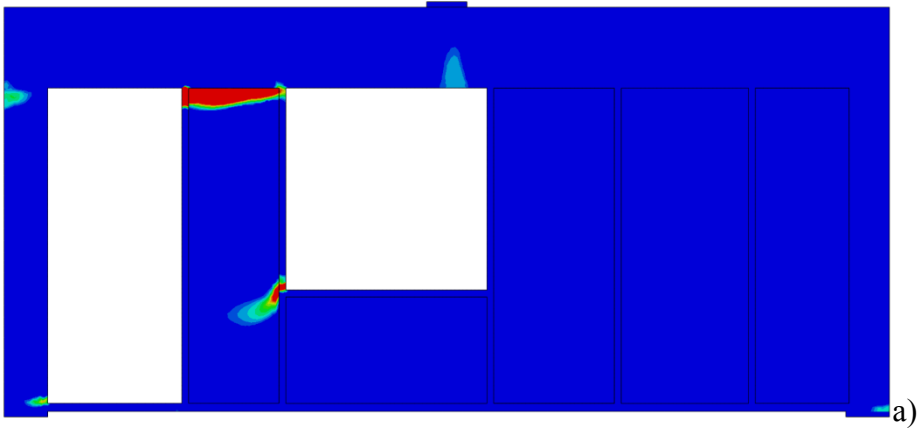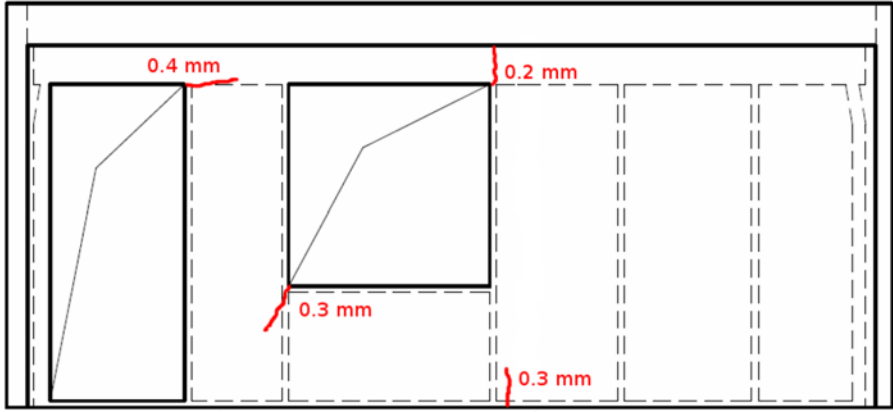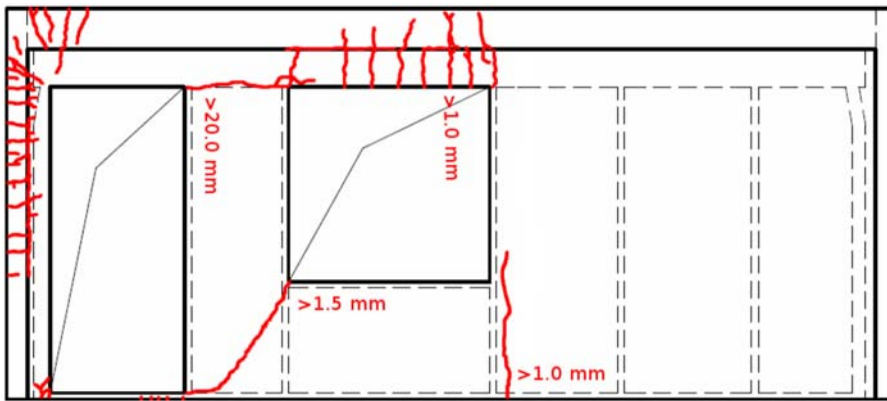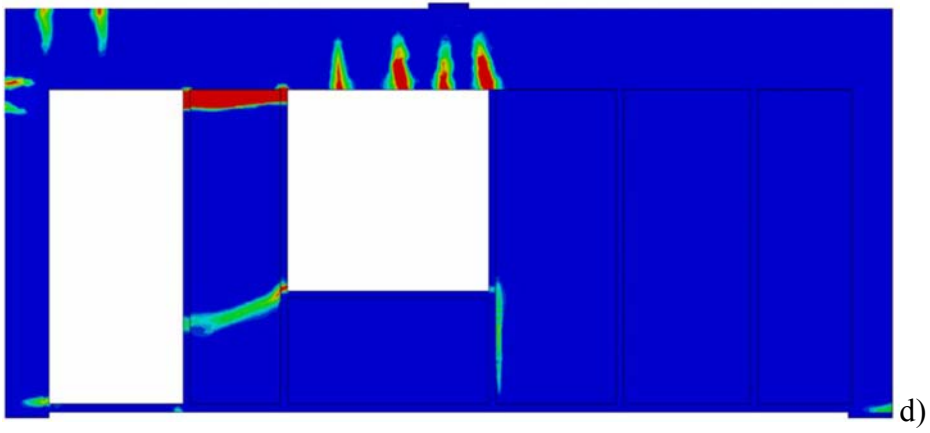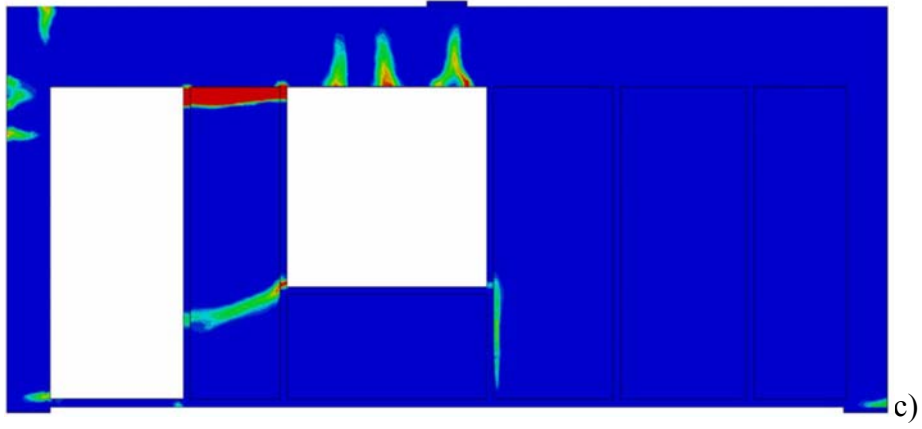
Fig.21: Comparison of calculated evolution of non-local tensile softening parameter κ_2 within enhanced elasto-plasticity in composite slab panel with experimental crack pattern for different vertical force F of Fig.20 (curves 'a' and 'b'): a) F=70 kN (u=1.83 mm), b) F=80 kN (u=2.19 mm), c) F=100 kN (u=4.32 mm, first peak in FEM computations), d) F=90 kN (u=5.86 mm, end of softening in FEM computations) and e) F_{max}=118 kN (failure, u=9.22 mm) (tensile fracture energy G_f=200 N/m (curve 'a' of Fig.17B), compressive fracture energy G_c=3250 N/m (curve 'b' of Fig.17A), bond-slip with u_0=0.03 mm and characteristic length of micro-structure l_c=5 mm)

FIGURE 21
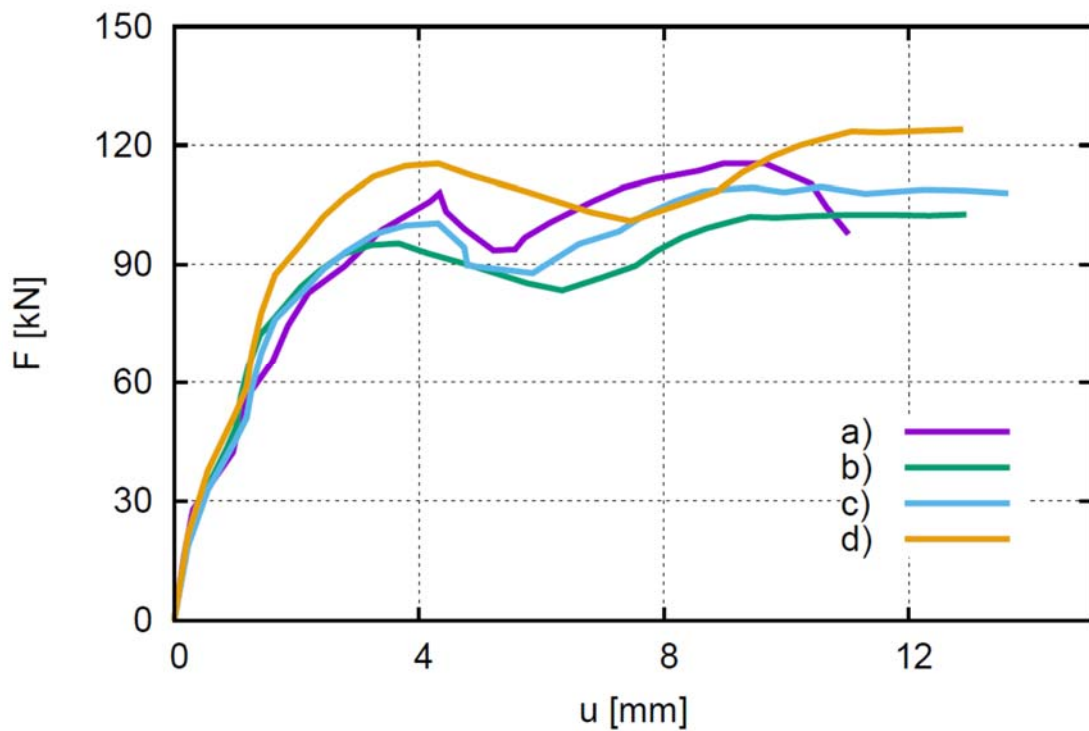
Fig.22: Vertical force-deflection curves $F=f(u)$ composite wall panel from FE analyses within enhanced elasto-plasticity with different compressive fracture energy G_c (tensile fracture energy $G_f=200$ N/m (curve 'a' of Fig.17B), bond slip with $u_0=0.03$ mm and characteristic length of micro-structure $l_c=5$ mm): a) experimental result (Fig.10), b) FEM with $G_c=2750$ N/m (curve 'a' of Fig.17A), c) FEM with $G_c=3250$ N/m (curve 'b' of Fig.17A) and d) FEM with $G_c=3750$ N/m (curve 'c' of Fig.17A)
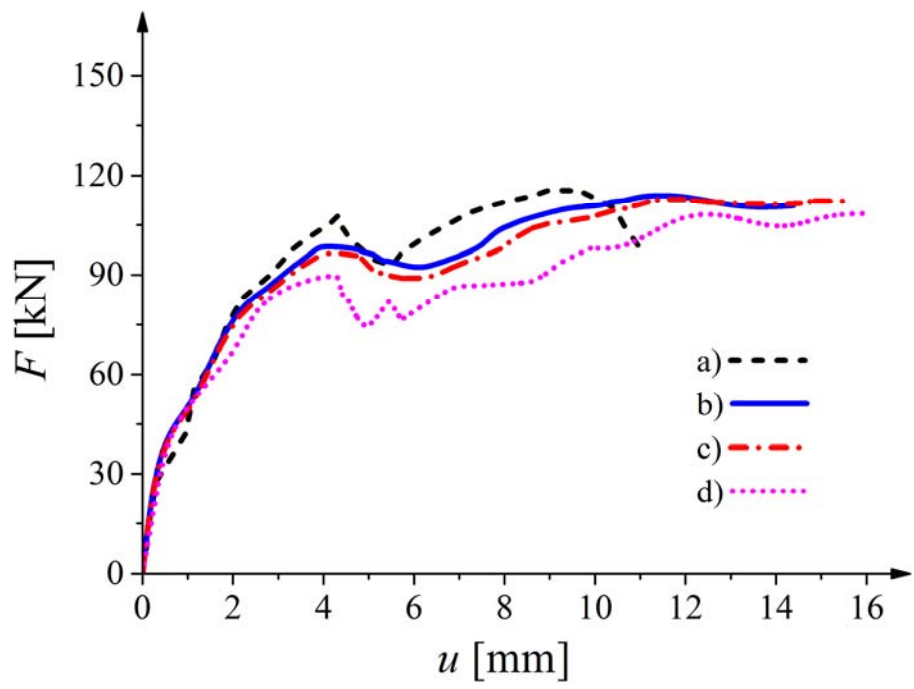
FIGURE 22
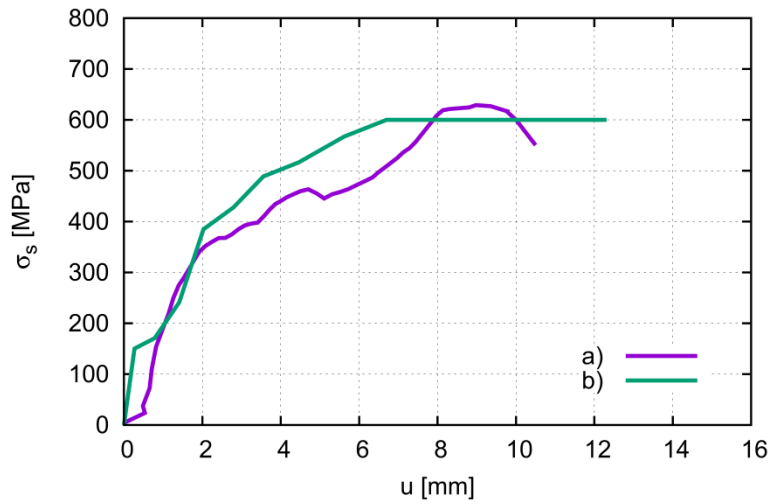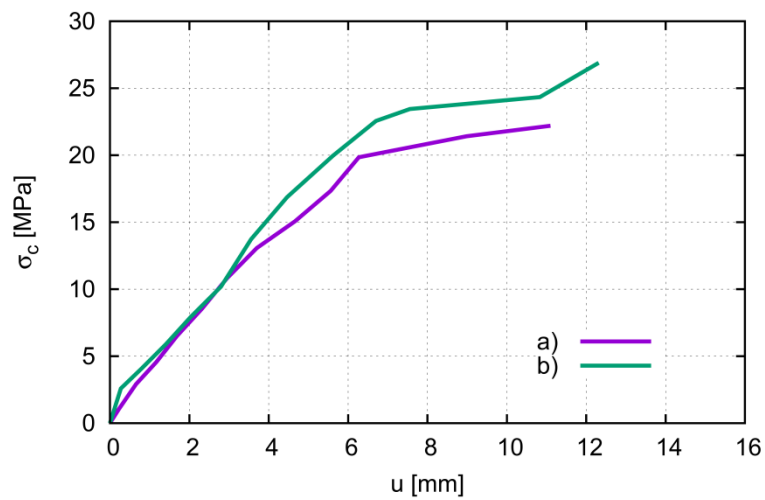
Fig.23: Calculated and measured normal stress σ at wall mid-span versus deflection u: A) tensile stress in reinforcement (before failure) at frame beam bottom and B) compressive stress in concrete at frame beam top and (a) experiments and b) FE result within enhanced elasto-plasticity (tensile fracture energy G_f=200 N/m (curve 'a' of Fig.17B), compressive fracture energy G_c=3250 N/m (curve 'b' of Fig.17A), bond-slip with u_0=0.03 mm and characteristic length of micro-structure l_c=5 mm)
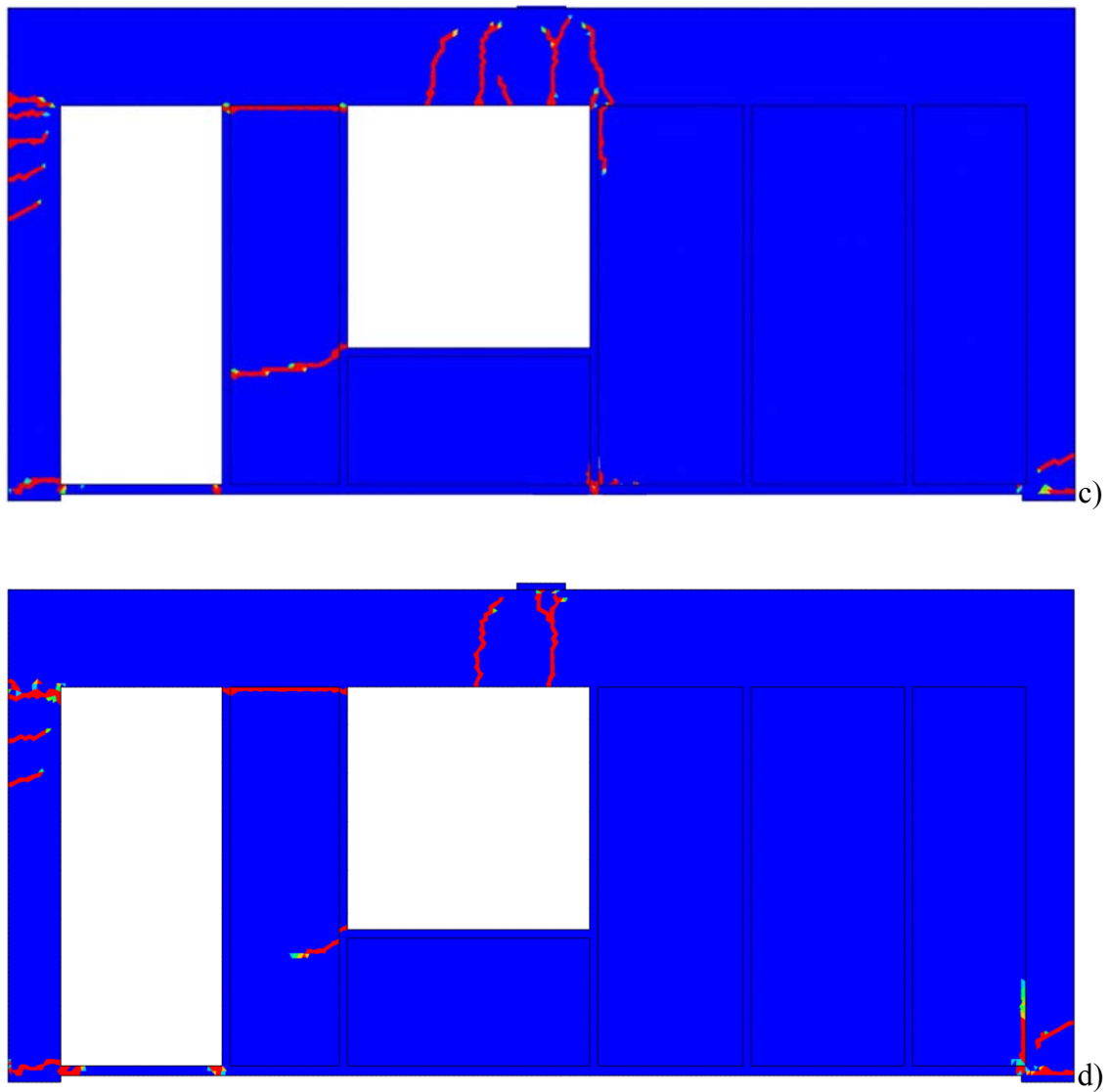
FIGURE 23

b)
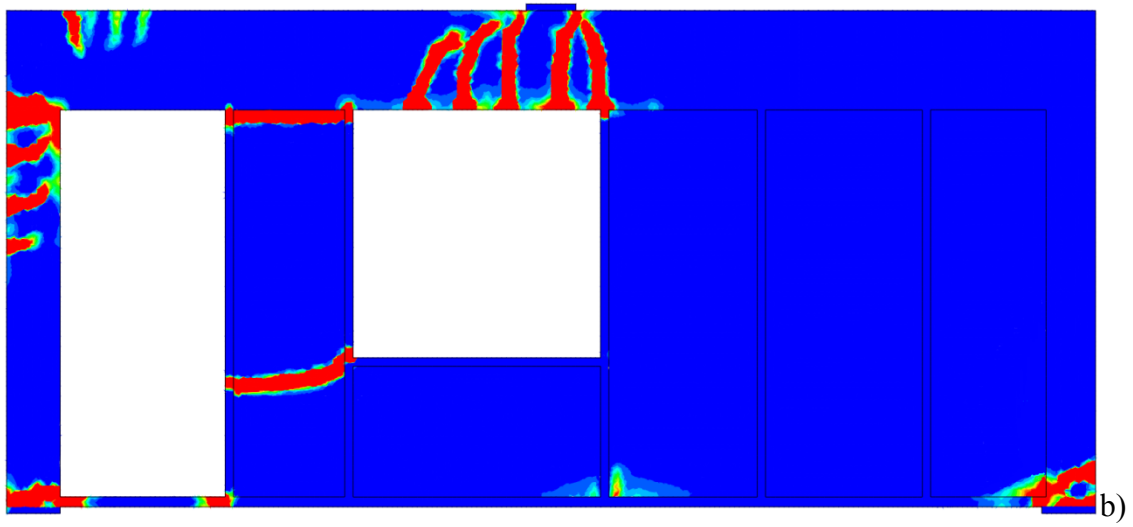
Fig.24: Calculated force-deflection curves and distributions of non-local/local equivalent strain measure (u=11 mm) for composite wall panel from FE analyses within coupled elasto-plastic-damage: a) experiment, b) non-local approach with l_c=5 mm, c) crack-band approach and d) local approach
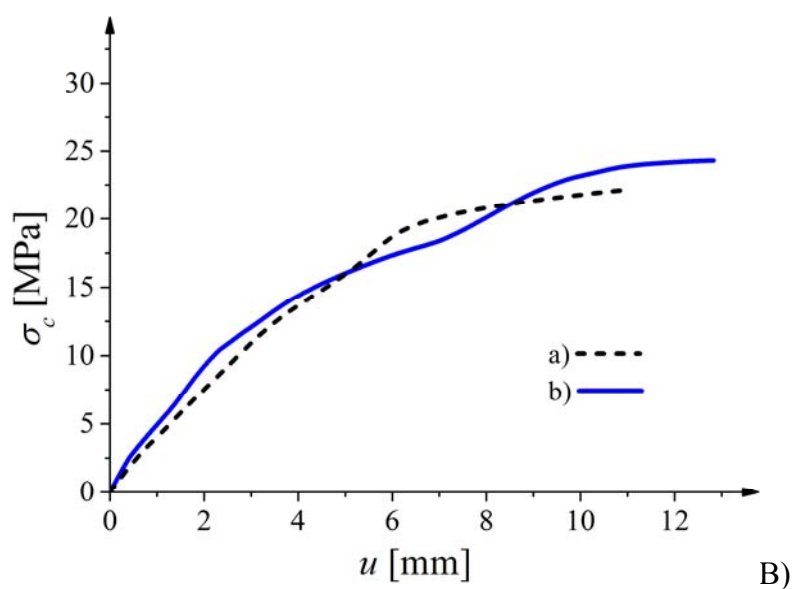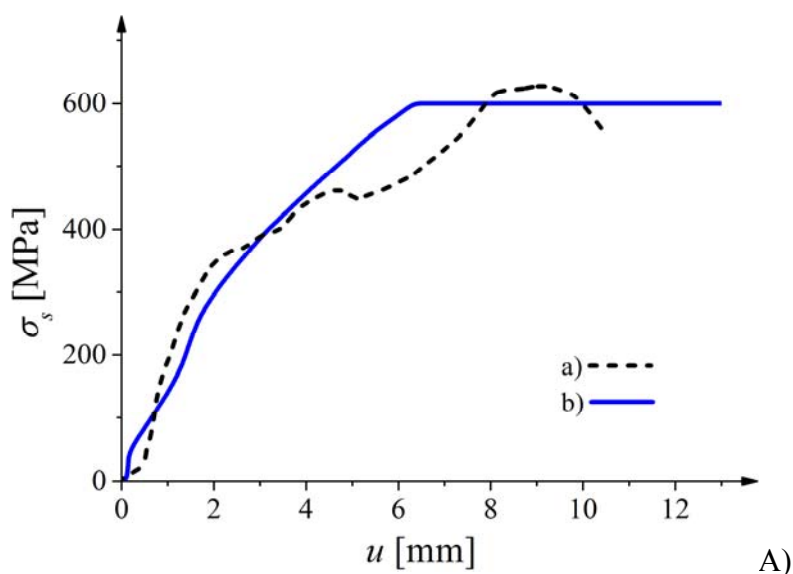
FIGURE 24

Fig.25: Calculated and measured normal stress σ at wall mid-span versus deflection u: A) tensile stress in reinforcement at frame beam bottom (until breaking) and B) compressive stress in concrete at frame beam top and (a) experiments and b) FE results within enhanced coupled elasto-plastic damage

FIGURE 25